Dipartimento di
Ingegneria Meccanica e Aerospaziale

Airbus Defence and Space gmbh

Corso di Laurea Magistrale in
INGEGNERIA AEROSPAZIALE

Electric Propulsion Diagnostic Package Development and Thruster Characterisation

Relatore accademico:
Prof. Lorenzo Casalino

Referente aziendale:
Dr. Franz Georg Hey
Dr. Oliver Mandel

Candidata:
Elena Germano
Mat. 290491

Anno accademico 2022-2023
Sessione di laurea Luglio 2023

Acknowledgements

Firstly, I'd like to express my thanks to my supervisor, Prof. Casalino, who has supported me throughout this research project.

I would like to express my gratitude and appreciation for Dr. Mandel whose guidance, support and encouragement has been invaluable throughout this study. I also wish to thank Dr. Hey for the trust he placed in me since the very beginning of this project.

Lastly, I would like to thank my friends, my family and my partner for standing by me and providing the support I needed throughout this time.

"There have to be bad days, otherwise the good days would be just average"

Abstract

The present work describes the process of revision and improvement of the micro-Newton thrust balance used by Airbus Defence & Space in Friedrichshafen for electric propulsion testing; in particular, the replacement of the interferometer device used to evaluate the differential translation between the two hanging pendulums of the thrust stand setup. The new device is assembled and the characterization is performed; the necessary hardware modifications are designed and implemented for installation inside the vacuum chamber.

The interferometer demonstrated the capacity for differential pathlength measurement, with a noise level under 1 $\mathrm{nm}/\sqrt{\mathrm{Hz}}$ between 3 mHz and 1 Hz, and the capacity for Differential Wavefront Sensing (DWS) is enhanced from the previous setup. The devices are able to hold an acceptable, and improved, level of contrast when transitioning from in-air to in-vacuum measurements.

It is expected that the new setup will improve the performance of the thrust balance apparatus by a substantial amount, and such verification is the natural prosecution of the present work.

Contents

List of Figures

List of Tables

Acronyms

AC	Alternating Current
AM	Amplitude Modulation
AOCS	Attitude and Orbit Control System
AOM	Acousto Optic Modulator
ASD	Amplitude Spectral Density
BS	Beam Splitter
CAD	Computer Aided Design
DC	Direct Current
DFT	Discrete Fourier Transform
DLL	Dynamic Link Library
DS	(Airbus) Defence & Space
DWS	Differential Wavefront Sensing
ESA	European Space Agency
EPL	ESA Propulsion Laboratory
GRACE-FO	Gravity Recovery and Climate Experiment Follow-On
ILR	Interferometric Laser Ranging
LET	Laboratory for Enabling Technologies
LISA	Laser Interferometer Space Antenna
MFD	Mode Field Diameter
NA	Numerical Aperture
NCO	Numerically Controlled Oscillator
OFMT	Optical Formation Metrology Testbed

OMT	Optical Metrology Terminal
OTS	Off The Shelf
PBS	Polarising Beam Splitter
PCB	Printed Circuit Board
PD	Photodiode
PER	Polarization Extinction Ratio
PLL	Phase Locked Loop
PSD	Power Spectral Density
QPD	Quadrant Photo Diode
TMS	Thrust Measuring System
USB	Universal Serial Bus
VCO	Voltage Controlled Oscillator
VI	Virtual Instrument

Chapter 1

Introduction

Electric propulsion uses electrical power to accelerate a propellant, employing different electrical and/or magnetic fields and techniques. The advantage of electric propulsion in comparison to the more traditionally used chemical propulsion is the higher exhaust velocity, and therefore the mass of propellant needed to accelerate the spacecraft is much lower. While the chemical thrusters are limited by the energy present in the propellant, electric propulsion is limited by the available electrical power on-board the spacecraft. The main consequence is that electric thrusters are suitable for low-thrust and long duration applications. Moreover, electric thrusters are suited for highly precise maneuvers, which explains their use in AOCS systems where precision is of the utmost importance; however, this property derives from the very low level of thrust that the device is capable of producing, which creates different challenges during the development and characterization phase.

When developing a new thruster, it is fundamental to evaluate its capabilities, first and foremost via direct thrust measurements. For chemical rockets, the method commonly used to measure thrust is a Thrust Measuring System (TMS), which is composed of load cells that evaluate the vertical movement derived from the firing of the thruster. Since the order of magnitude of the thrust expressed by electrical thrusters is in many cases smaller than what can be achieved by chemical thrusters, the tools to inspect, assess and characterize an electrical thruster need to be different. In Europe, only a few facilities are able to perform the necessary tests on micro-Newton thrusters, and even fewer can achieve testing in the sub-micro-Newton regime.

One of such facilities is the Laboratory for Enabling Technologies in Friedrichshafen; the facility consists of a vacuum tank, a highly precise thrust balance, a plasma diagnostic setup and all the necessary hardware to perform tests and develop innovative thrusters. In particular, the facility was designed to be able to test thruster candidates for the Attitude and Orbit Control System of the scientific space mission LISA (Laser Interferometer Space Antenna).

The objective of the LISA mission is to act as a gravitational wave detector in space, to avoid the seismic noise background present in measurements collected with instrumentation on the Earth's surface. The mission architecture consists of three identical satellites that form a three armed interferometer in space; the constellation allows for the measurement of the variation of the distance between free-falling test-masses onboard the satellites in the pico-meter regime. The constellation orbits at a distance of 1 AU in a heliocentric orbit, within 20 degrees of the Earth; this orbit was selected to grant optimal communications with the ground stations, a stable formation with minimal variation of the inter-spacecraft angles, excellent power generation capabilities and minimum ΔV. Given the extremely high precision required for the distance measurements, external disturbances must be counteracted by a proper AOCS, which necessarily implies the use of micro-Newton thruster systems. The main source of disturbance is constituted by the solar pressure, which amounts to about 10 μN per thruster; the complete requirements impose a minimum thrust of 0.3 μN and a maximum thrust of 100 μN. Internal gravitational balancing residuals might require an additional permanent acceleration of up to 1 nm/s^2. [25]

During the assessment of an innovative thruster, a thrust balance is often used. For instance, the ESA Propulsion Laboratory (EPL) in Noordwijk has multiple devices available, which allow for testing of a wide range of thrusters. More details are summarised in Table 1.1.

The facility in Friedrichshafen is not as large, only having one thrust balance available;

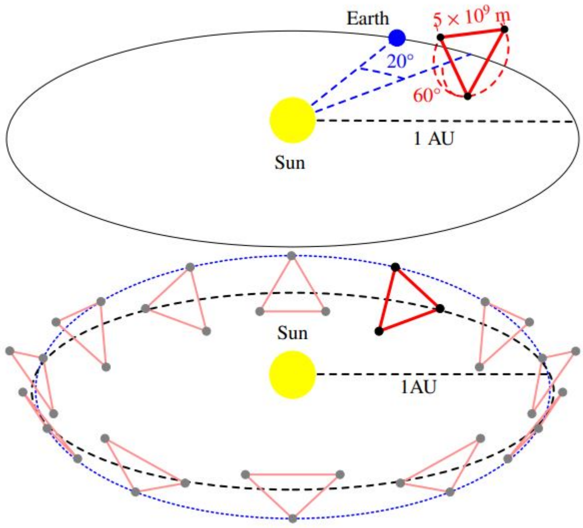

Figure 1.1: Sketch of the LISA orbit. The satellites form an equilateral triangle in a heliocentric orbit. The formation follows the Earth's orbit within 20°, which corresponds to approximately 50 million kilometers. The orbit enables an optimal data transmission to Earth and power generation as well as low gravitational effects caused by the Earth and other space bodies. Moreover, the ΔV required to reach the final orbit is minimised. [25]

however, the results obtained with the device present in the vacuum chamber of the laboratory are consistent with the requirements under which the facility was designed. Performing a comparison with the devices listed in Table 1.1, Airbus DS's thrust balance achieves a range of 0-4800 μN and a resolution under 0.1 μN. [24]

Some issues arose with the correct operation of the setup, solving which is the purpose of the present work.

1.1 State of the art

In general, pendulum thrust stands are regarded as quite reliable when it comes to directly measuring the thrust generated by electric thrusters; the use of such devices instead of the more traditionally used load cells is mainly tied to the lower thrust-to-weight ratios. The pendulums have three main configurations (hanging, inverted and torsional), each with advantages and disadvantages, but overall equivalent. Aside from the chosen architecture, a pendulum thrust stand requires displacement sensors, spring elements and/or dampers; amongst the most used sensors are optical interferometers, especially in applications where the expected displacements are small, since they provide high sensitivity and resolution. [2]

	Range	Uncertainty	Resolution
Alta 1-axis optical thrust stand	5-500 mN	±2 mN	Variable
Alta Low thrust balance	0.2-10 mN	±0.2 mN	Variable
Mettler-Toledo AX504	500 g ≡ 5 N	±10 µN	0.1 mg ≡ 1 µN
Mettler-Toledo XP2004S	2.3 kg ≡ 23 N	±10 µN	0.1 mg ≡ 1 µN
NPL micro-thrust balance	1 µN-1 mN	±0.1 µN	0.1 µN

Table 1.1: EPL Thrust balances [1]

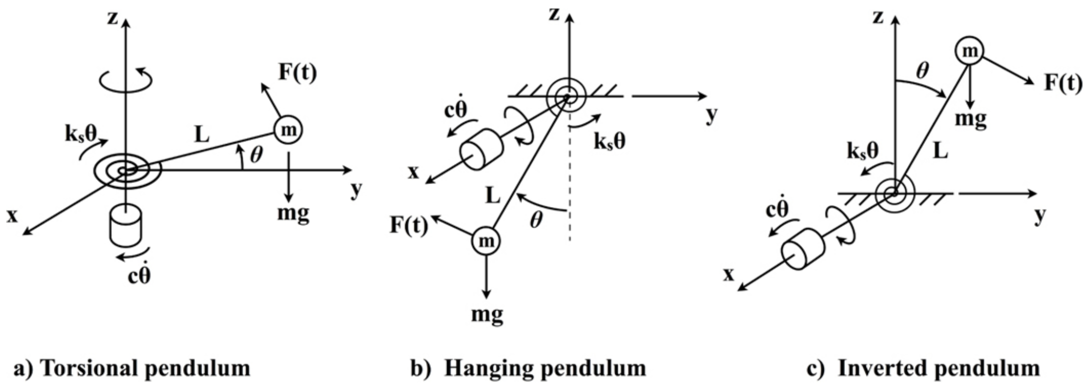

Figure 1.2: Synthesis of the three main types of thrust balances. The torsional pendulum rotates on an axis that is parallel to the gravity vector, while the inverted and hanging pendulum both use a perpendicular axis. [2]

The simplest architecture for an inverted pendulum thrust balance involves a vertical arm that is connected to a hinge on the bottom side and has the thruster connected at the top; this configuration allows for a reduction of the spring constant of the pendulum arm, since the thruster produces a certain torque that counters the spring torque of the arm itself. However, this kind of disposition is prone to problems when the inclination in respect to the gravity vector changes, requiring in many cases a dedicated system that actively controls the deviation. [2]

A different approach is taken with torsional balances, since in this case the rotational axis of the pendulum is parallel to the gravity vector; this attribute allows to separate the response from the thruster mass, making them appropriate for a wide spectrum of thruster weights. Torsional balances provide good results for micro-Newton levels of thrust and impulse measurement; it has recently been shown that one such device is capable of providing a resolution between 0.09 μN and 0.21 μN in the range between 2.5 μN and 27.8 μN, with good linearity in the range between 2 μN and 30 μN. [2,3] Another similar device was also recently tested, demonstrating the capacity to operate in open loop (the pendulum is left to freely move and the angle caused by a known force is measured) and closed loop (the pendulum is kept in position by applying a force to contrast the external action), and it demonstrated linearity in the range 0-200 μN with a resolution of 0.1 μN. [4]

The easiest solution to implement is the hanging pendulum architecture, which consists of a top hinge connected to a vertical arm with the thruster on the opposite end; in this case, the gravity torque continuously operates to move the pendulum back to the resting position. This design comes with some compromises in volume and sensitivity, since the low thrust generated by electric thrusters often results in small deflections of the pendulum; however, if designed taking into consideration the control of external noise sources, they are capable of producing high resolution measurements. [2]

One such device was recently developed using a rectangular frame suspended by two berillium copper strips; this apparatus is directly calibrated using gravity, and its stiffness can be adjusted by modifying the center of mass. Such a device achieved a measured thrust increment of 0.09 μN with an uncertainty of 0.02 μN, and a measuring range up to 1000 μN. [5]

For the thrust balance in Airbus DS, the main way in which the external disturbances are suppressed is by having a double pendulum. The thrust measurement is derived from a differential displacement measurement, and the theoretical resolution that can be achieved is under 0.1 μN, with a thrust range of 0-4800 μN. [24]

1.2 Purposes of the present work

As previously mentioned, the testing facility at Airbus in Friedrichshafen consists mainly of a vacuum tank, a highly precise thrust balance and a plasma diagnostic setup. In particular, the thrust balance was developed within the PhD thesis of Dr. Hey [24], and has achieved the requirements imposed by missions such as LISA. The core principle of the thrust balance is to evaluate the differential translation between the two pendulums using an interferometer, since it allows for appreciation of the small displacements caused by the very low thrust expressed by the devices being tested.

Though the current facility is successfully performing a number of test campaigns on different thrusters, an issue emerged regarding the interferometer used to calculate the differential measurement. As it will be covered in the following chapters, the interferometer currently being used is composed of a series of optical components which are mounted on supports inside a protective cover connected to the chamber's internal support structure. The instability in the mounts causes problems with the alignment of the optical components, and therefore hinders the performance of the diagnostic setup. As a matter of fact, it is often required to open the vacuum chamber to be able to adjust the alignment, which is very time-consuming and a nuisance for the performance of the test campaigns.

Thus, the interferometer needs to be substituted with a different device, which decreases the incidence of these criticalities. Such a device had already been designed for another purpose within the Laboratory for Enabling Technologies; the aim of the present work has been the realization of the tool, and the design and integration inside the vacuum chamber.

1.3 Layout of the present work

When documenting the process of the present work, it was deemed most natural to first describe the integration process that allowed to obtain the interferometer device, and then to detail the insertion of the new interferometer setup in the thrust balance structure. Therefore, one chapter will be dedicated to the interferometer assembly process, with all optimizations and corrections, and to the design of the cover for the protection of the optical components. The following chapter will detail the design and realization of the improved thrust balance during the substitution of the interferometer setup. Finally, one chapter will be dedicated to the conclusions derived from the present work and possible expansions on the technology used.

The division of the chapters was made on the basis of topic rather than a temporal succession; the activities described in this thesis were for the most part simultaneous and developed over the course of several months.

Chapter 2

Interferometer integration process

Interferometry is the use of the interference of superimposed waves to extract information. One of the most useful applications of such a technique is the measurement of extremely small displacements; light from a single source is split into two beams that travel in different optical paths, and are then recombined to produce interference.

When two waves of the same frequency combine, the resulting intensity pattern is determined by the phase difference between the two waves. Waves that are in phase will undergo constructive interference while waves that are out of phase will undergo destructive interference. Waves which are not completely in phase nor completely out of phase will have an intermediate intensity pattern, which can be used to determine their relative phase difference.

Typically, a single incoming beam is split into two identical beams by a beam splitter; each beam travels a different route, called a path, and they are recombined before arriving at a detector. The difference in the distance travelled by each beam creates a phase difference between them. [6]

Heterodyne detection employs a dual frequency laser source; this creates a beat frequency between the two beams, given by the difference between the frequencies. The advantage of this technique is the linear and continuous correlation between the beat frequency and the velocity of the reflector, allowing for the achievement of high-resolution position sensing without the requirement for a stable measurement of signal voltage. Moreover, the sign of the phase difference can easily be determined. [7]

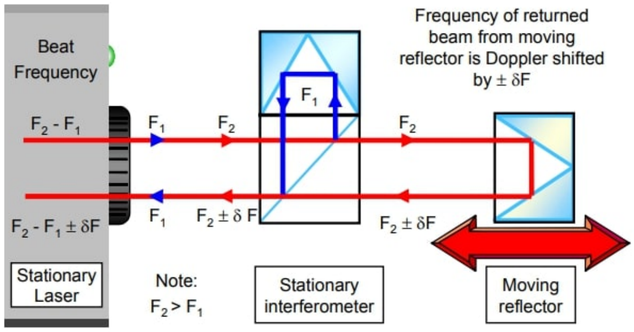

Figure 2.1: The laser source emits two beams, one with a frequency F_1 and one with a frequency F_2. The resulting beat frequency is $F_2 - F_1$. The beam with frequency F_1 is reflected into the reference path, while the beam with frequency F_2 goes on to strike the moving reflector, and undergoes a Doppler shifted reflection in the magnitude of $\pm\delta F$. When combined with the F_1 frequency light at the interferometer, it results in a new beat frequency. [7]

2.1 Resulting device and methodology

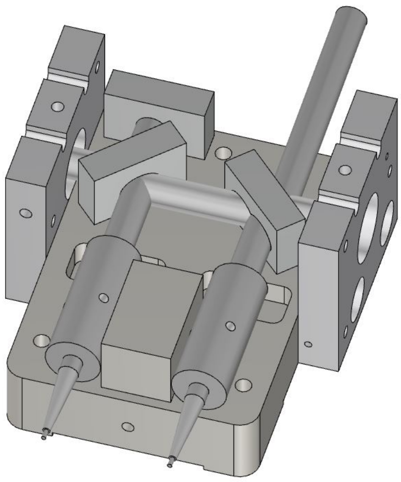

Figure 2.2: The resulting device, without the cover and with the trace of the beam paths. The right beam leaves the interferometer to reach the moving reflector, and therefore provides the measurement; the left beam is used as reference, and when superimposed to the right generates the interference that is detected by a quadrant photodiode mounted on the right side. [21, 22]

The final device resulting from the integration process is depicted in Figure 2.2, although the picture is missing the two printed circuit boards (PCBs) mounted on either side and the protective cover (which will be described in the following sections). Comparing the architecture of the device to the principle of operation depicted in Figure 2.1, it can be noticed that the beam originating from the right fiber launcher is the measurement beam, which leaves the interferometer to be backreflected by the moving mirror; the beam originating from the left fiber launcher, instead, is used as reference. The two beams are superimposed, and the result of such interference is detected by a quadrant photodiode mounted on the right side.

In the following sections, the integration process of the interferometer will be briefly outlined, and all the components will be described. The flowchart summarizes the main steps and the logical connections between them.

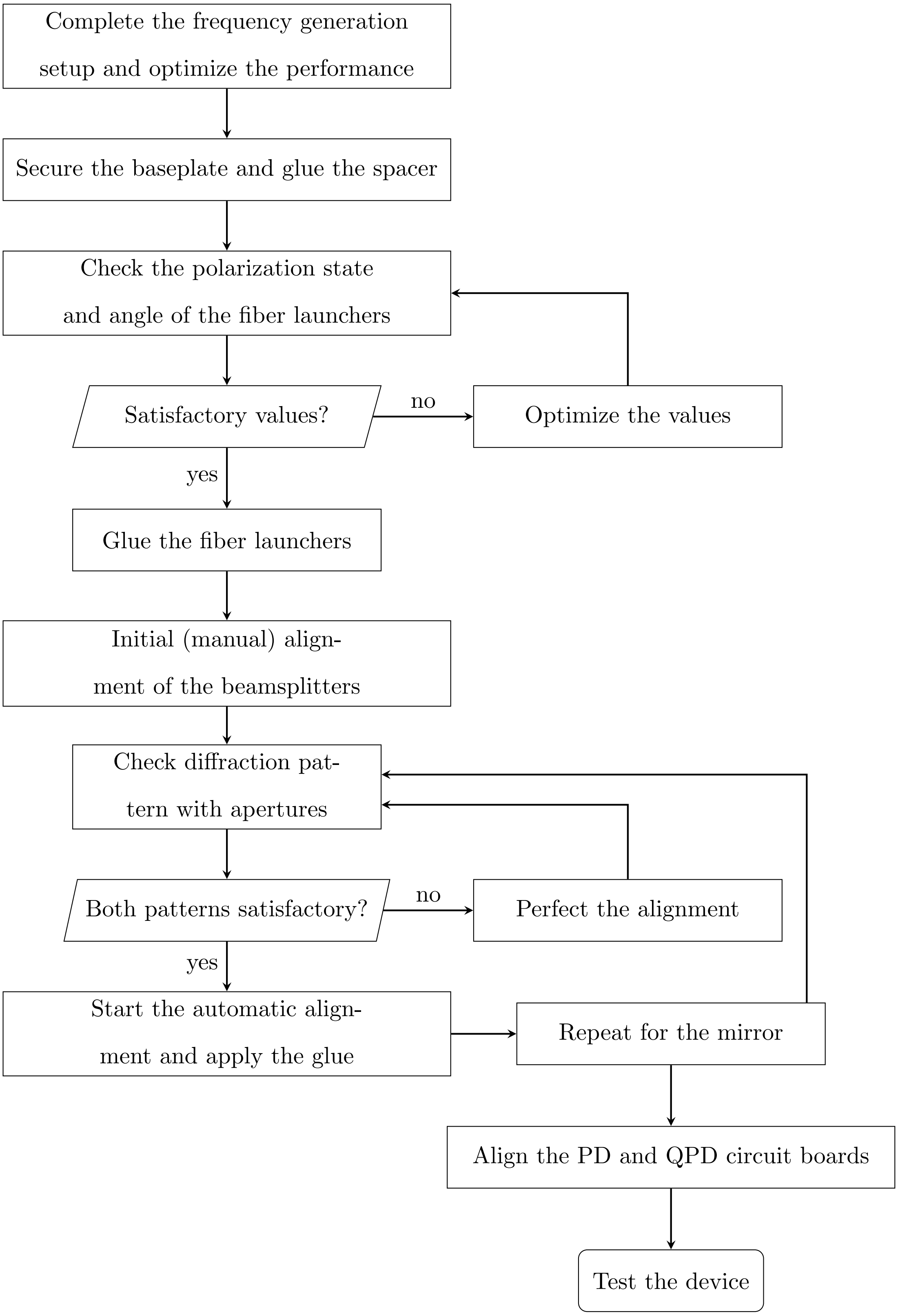
Complete the frequency generation setup and optimize the performance
Secure the baseplate and glue the spacer
Check the polarization state and angle of the fiber launchers
Satisfactory values?
no
Optimize the values
yes
Glue the fiber launchers
Initial (manual) alignment of the beamsplitters
Check diffraction pattern with apertures
Both patterns satisfactory?
no
Perfect the alignment
yes
Start the automatic alignment and apply the glue
Repeat for the mirror
Align the PD and QPD circuit boards
Test the device

2.2 Frequency generation

In order to obtain heterodyne detection, a proper frequency generation setup is needed. The optical setup is responsible for the separation of the laser beam into the reference and the measurement beam, for the shift in frequency that allows to achieve the correct beat signal and for the coupling of the beams in the optical fibers that carry them to the device depicted in Figure 2.2.

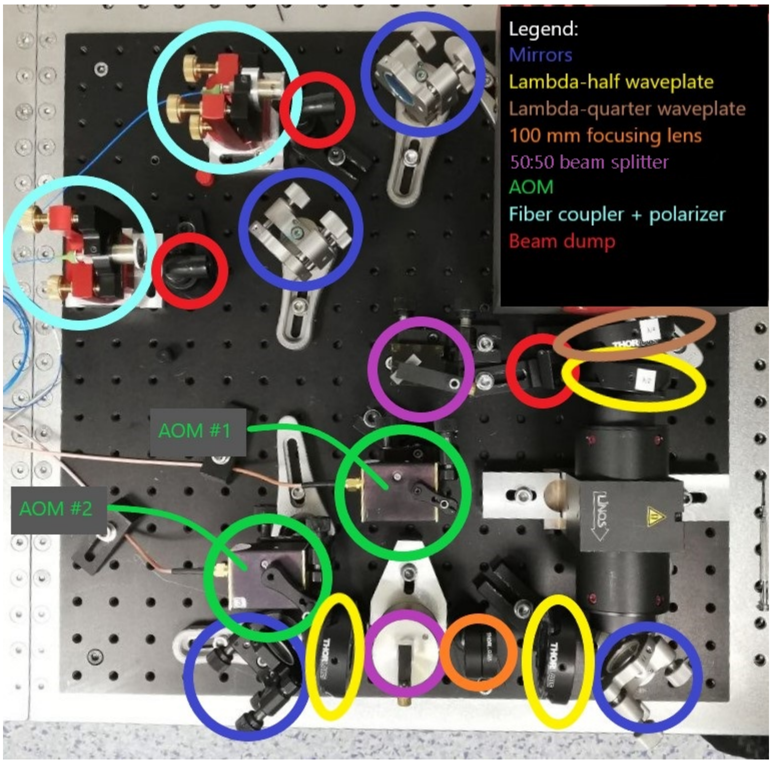

Figure 2.3: Heterodyne frequency generation optical setup. The generated laser beam is appropriately focused using a lens, then split using a cube beamsplitter. Each beam enters an Acousto-Optic Modulator, which shifts the frequency of the beams; it is here that the beat frequency is generated. The two beams are then coupled inside the optical fibers using two fiber collimators, each provided with a polarizer.

The laser generation emits a laser beam at a wavelength of 1064 nm. Its characteristics are summarized in Table B.1. It can also be noticed that the temperature of the laser crystal is kept at 27 °C; this allows for the laser generation to maintain a linear characteristic between the laser frequency and the temperature, minimising the risk of mode jumps. The current used is around 80% of the nominal value, as to not generate instability.

The laser beam exiting the laser generation encounters a series of waveplates, which ro-

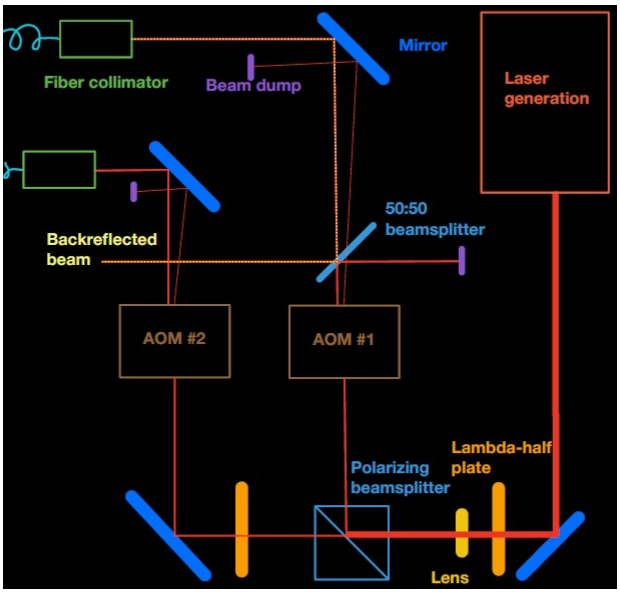

Figure 2.4: In this illustration, the path of the beams can be seen in more detail; it is possible to see the zero-order beam generated by the AOMs (which is discarded) as well as the first order, which is coupled into the fiber. The yellow dotted beam is the backreflection of the measurement beam that couples back into the fiber; it is used as an indication of the quality of the alignment, by measuring the differential power with a powermeter.

tate the polarization state to achieve a vertically polarized light. This process is necessary to allow for the correct operation of the Acousto-optic modulators (AOMs). [8]

The choice of the focal length for the lens is critical to the success of the frequency generation; multiple values of such parameter were tested. Ultimately, best results were achieved with a focal length of 100 mm; this particular length allows for the beam to be focused in close proximity to the inlet of the acousto-optic modulators, and it also creates a beam diameter close to the required value at the inlet of the fiber collimator.

To obtain the two separate beams that are needed for the interferometer, a polarizing cube beamsplitter is used. The cube architecture allows for the optical paths of the two beams to remain of equal length, with no beam shift; the splitting ratio is determined by a $\lambda/2$ plate. [9]

The beams then enter the acousto-optic modulators, which provide the controlled shift in the frequency. This component's principle of operation is based on the acousto-optic principle, which is the change in refractive index of a material when a sound wave provokes a oscillating mechanical strain. This effect is used to either increase or decrease

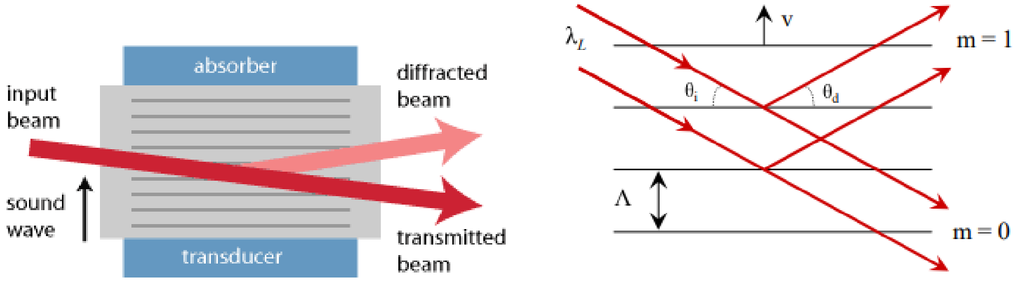

Figure 2.5: Principle of operation of an acousto-optic modulator; the horizontal lines represent the areas of different refractive index caused by the acoustic wavefront. The incoming laser beam is therefore scattered on the different interfaces, causing the wanted shift in frequency. [10, 11]

the frequency of the incoming beam by the frequency of the sound wave. The behaviour of the component is depicted in Figure 2.5. In particular, the beam scattering into an angle of $2m\theta_d$ corresponds to absorbing or emitting m phonons. The change in frequency of the input beam can therefore be written as

$$\Delta f = \frac{mE_{phonon}}{h}. \tag{2.1}$$

m can be positive or negative, which corresponds respectively to an increase or a decrease of the input frequency by the frequency of the sound wave. [10, 11]

In the particular case of the presented setup (refer to Figure 2.3 and 2.4), the frequency for the beam exiting AOM #1 is set to be 80.00 MHz, while the beam exiting AOM #2 is shifted to a frequency of 80.01 MHz; this creates a beat frequency of 10 kHz. However, it is possible to modify the beat frequency to virtually any value; for example, a beat frequency of just 1 Hz allows for the interference pattern to be visible by the naked eye, which is particularly useful in other parts of the process.

Between AOM #1 and the next components, a 50:50 beamsplitter is added; this component, again, divides the incoming beam into two equal halves, one of which proceeds to the fiber coupler. The other half, instead, will be discarded.

Finally, it is necessary to couple each beam in the corresponding single-mode, polarization maintaining optical fibers; the objective of such optimization is to maximize the coupling efficiency, or the ratio between the power of the light entering the fiber and the power of the source.

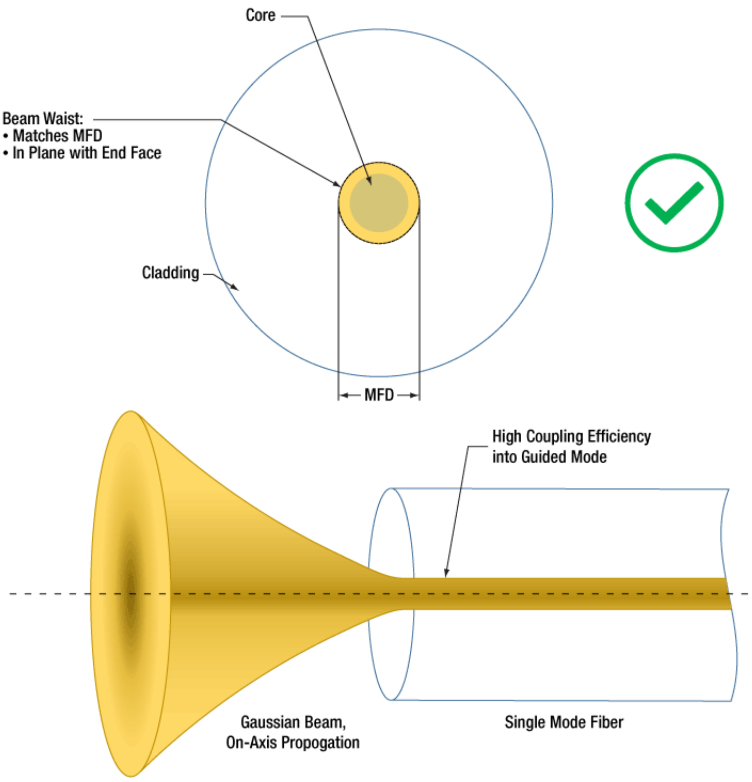

Figure 2.6: Ideal beam position and dimension for a successful coupling. The coupling efficiency can be affected by multiple factors, including the angle of incidence of the beam and the beam size, shape and position in respect to the fiber core. In particular, it is helpful to match the beam waist to the Mode Field Diameter (MFD), or the radial position where the intensity of the beam reaches a value equal to e^{-2} times the peak intensity. [12, 13]

The process of maximizing the coupling efficiency required the connection of the optical fiber to a powermeter, in order to follow the evolution of the power entering the fiber as the optimization was proceeding. Then, both the coupler mount and the mirror in front of it were adjusted using the provided screws on the respective structures, to achieve the best possible incidence angle and position for the beam on the inlet of the optical fiber. When this was not enough, it was decided to add the translation of the focusing lens within the fiber collimator, in order to allow for the beam to be focused as close as possible to the entrance of the fiber.

It is important to note that the choice for the focal length of the focusing lens between the laser generation and the beamsplitter, as previously discussed, is influenced by the need to achieve the collimated beam diameter shown in Table B.2.

The fiber couplers are fitted with a polarizer, which hindered the coupling efficiency by as much as 20%; however, they are necessary to correctly direct the laser beam into the polarization maintaining fiber. Moreover, the setup is balanced, in the sense that the coupling efficiency is similar for both beams.

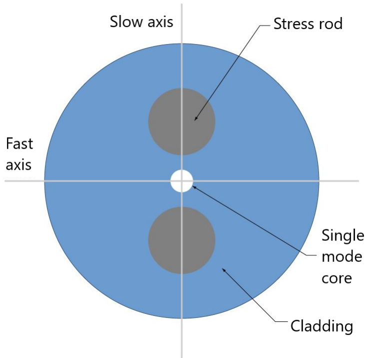

Figure 2.7: Illustration of the internal structure of a polarization-maintaining fiber; in particular, a PANDA fiber. It can be noticed that two glass structures, called rods, apply stress to the fiber core during the cooling process, and therefore cause the difference in propagation constant that allows for the fiber to maintain the incoming polarization (provided that the incoming beam is correctly aligned). [14]

The used fibers are polarization-maintaining, single mode fibers; in these fibers, stress elements are added to the fiber cladding, because mechanical stress causes birefringence in the glass. This characteristic means having two different propagation constants for the light inside the fiber, and therefore a barrier is created for propagation in a different axis. The most usual configuration is light being coupled in the slow axis, since it is less sensible to fiber bending. It is necessary to correctly align the fiber core to the laser beam from the source, for which a polarization analyzer is used. [14, 15]

The original design for the interferometer integration process called for an additional fiber between the fiber collimator and the fiber connected to the fiber launcher. The advantage of such a setup would be reducing the number of insertions of fibers into the fiber collimators, and therefore limiting the possible alignment problems. However, it was discovered that the available fibers were damaged, and, in the absence of a replacement, it was decided to directly connect the fiber going to the fiber launcher on the baseplate with the fiber collimator.

This necessary solution caused the repetition of the alignment procedure of the incoming beam for each insertion of the new fiber, as the delicate balance would be disrupted by the mechanical connection. The derived advantage is the possibility to better compensate the orientation of the slow axis for the pigtail fibers.

2.3 Alignment and bonding of the optical components

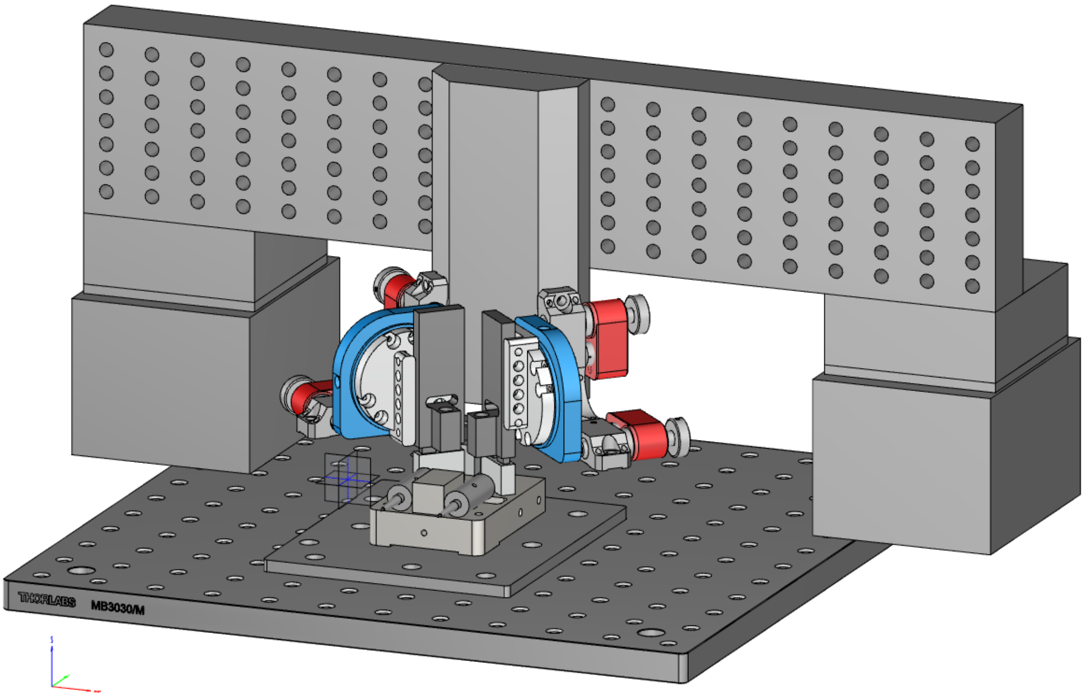

Figure 2.8: CAD view of the setup used to align and subsequently glue the components of the interferometer. In particular, special attention must be given to the mounting mirror structure, that allows for the automatic alignment of both the beamsplitters and the mirror. [21, 22]

The first step in the process of aligning and bonding all the components to the baseplate was to connect the very same baseplate to the baseplate adapter; this adapter provides the correct alignment, when employed with a certain number of posts appropriately placed (visible in Figure 2.10). The baseplate adapter, once aligned, was screwed on the breadboard underneath.

To proceed with the alignment of all optical components that would make up the interferometer, it was necessary to start by positioning the collimator spacer; this component would provide support for the next phase. A template was used to position the spacer at the correct distance from both sides of the baseplate. The employed adhesive has the characteristics summarized in Figure 2.9 and in Table B.3; in particular, the behaviour that the adhesive shows when temperature increases is fundamental for the beamsplitter alignment and integration process, but is also important in the event of a removal of some parts being required, as the glue can easily be brought to degradation temperature using a hot air device.

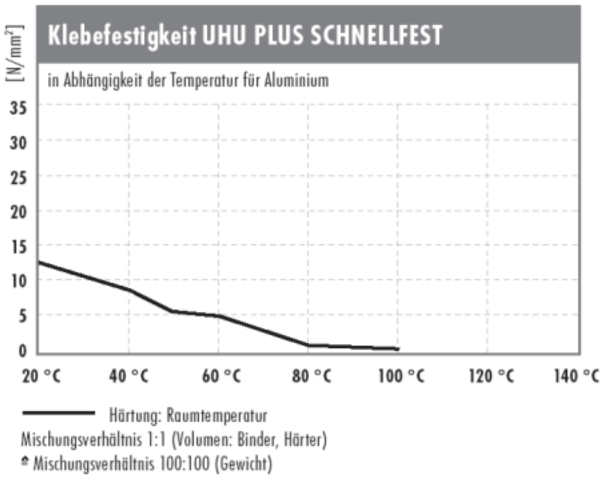

Figure 2.9: UHU Plus Schnellfest adhesive strength as a function of temperature [17]

Before the fiber launchers could be attached to the baseplate, their polarization state was analyzed in order to determine the correct angular position. Since the alignment procedure employs mirrors, the wanted polarization state was the so-called *vertical*; moreover, since the quality of the alignment is important, an optimization was performed in order to minimise the radius of the circle traced during the analysis. The radius of the circle visible in Figure 2.12 is determined by the angular position of the polarizer mounted on the fiber collimator; an optimization was performed for this property in order to minimise the variance from the mean polarization state, represented by the center of the circle. Then, the fiber launcher on the baseplate was rotated on its major axis to achieve a mean polarization state as close as possible to the wanted one. In order to trace the circle, the fiber core needs to be subjected to a source of stress; this stress can be mechanical, i.e.

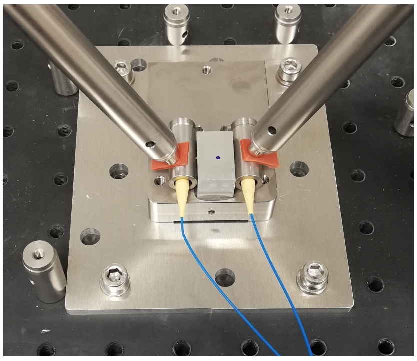

Figure 2.10: Detail on how the fiber launchers are kept in place during the gluing process. The tool in Figure 2.11 is fitted to the front portion of the fiber launchers and it allows for the rotation around their main axis, to adjust the polarization. It is also possible to notice the distribution of the metal posts that consents the correct alignment of the baseplate adapter. [21]

gently bending the fiber, or thermal, i.e. using the heat produced by the hands to modify the fiber equilibrium. [16]

It was deemed necessary to also be able to perform such optimization during the initial phase of the curing process of the chosen adhesive, and for this end a specific tool was designed and 3D-printed. The tool would be also fitted with a strip of silicone, to protect both the external surface of the fiber launcher and the internal surface of the tool itself, and to provide the necessary grip between the two surfaces. Two such tools were printed; however, defects arisen during the manufacturing process made it so that only one of the tools could be used in the adjustment process. Therefore, it was not possible to perform the alignment and integration procedure for both fiber launchers at the same time, but it was instead necessary to wait until the adhesive had reached an acceptable level of strength on the first one before it was possible to remove the tool and use it for the second launcher. In the case of the UHU Plus Schnellfest, it was better to wait at least 120 minutes [17]. Moreover, following the printing process the tools presented with a defect in the circular part; here, there was a notable separation between layers. This defect caused the tool to be damaged as a result of the stress applied to insert the fiber launcher; in the future, it would be recommended to print such tools paying particular attention at the layer distribution in this section of the piece.

Figure 2.11: Design of the tool used to adjust the angular position of the fiber launchers after the application of the adhesive, to optimize the polarization state of the laser beam.

One critical part of the setup is the out-of-plane displacement of the beam; unlike the in-plane displacement, this error has a very limited range of improvement by adjusting the motorized optic mounts (which affect the position of the beamsplitters), and therefore requires a closer attention and minimising before the components are glued in place. The proposed solution is the addition of an aluminium strip under the fiber launcher to partially compensate the inclination. It is preferable that the angle with the optical plane does not exceed 0.5 mrad; it is also best that the out-of-plane angle difference between the two beams stays below the same value, since higher angles could not be compensated by the beamsplitters.

The procedure, after applying the adhesive to the fiber launcher and positioning it, entailed measurements of the polarization state and of the out-of-plane displacement. For the former, non satisfactory values could be improved upon using the tool depicted in Figure 2.11, while for the latter the only applicable solution was the removal of the applied adhesive, another iteration of measurements followed by the addition of the necessary number of aluminium strips, and only then applying a new layer of glue. It is important to notice that, during the curing process, the adhesive could undergo physical changes in volume, and therefore the measurements of both polarization state and out-of-plane angle must be performed again after the appropriate time.

Following the gluing process, the results for the first interferometer are as depicted in Table 2.1 and Figure 2.12.

	Right launcher	Left launcher
η (°)	1.5	-2.1
$\Delta\eta$ (°)	1.8	2.7
ϕ (°)	-0.3	0.3
Mean PER (dB)	31.4	28.7
Min. PER (dB)	24.6	21.6
Out-of-plane angle (mrad)	-0.053	-0.26

Table 2.1: Results of the measurements performed after the fiber launchers were attached to the baseplate and the adhesive had completed the curing process. The quality of the alignment and the out-of-plane misalignment are satisfactory.

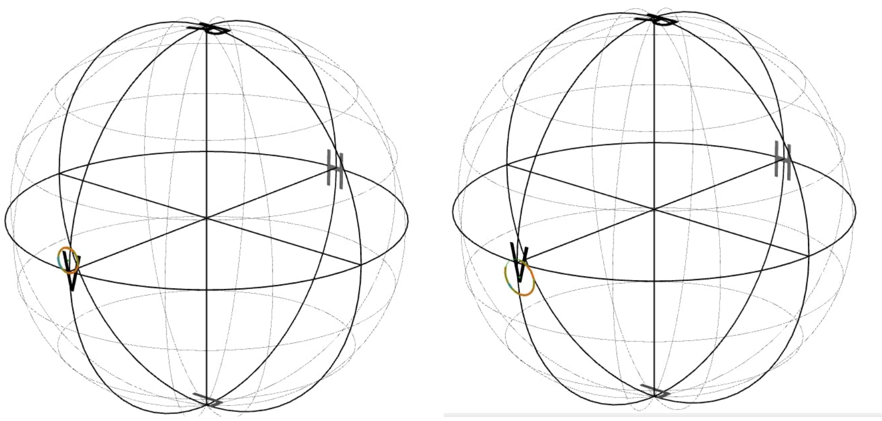

Figure 2.12: Results of the measurement performed with the polarization analyzer after the fiber launchers were attached to the baseplate and the adhesive had completed the curing process. The quality of the alignment is satisfactory, as can be noticed by the small radius of the circle. The image depicts, respectively, the beam exiting the right and left launcher.

The most critical part of the alignment is the optical alignment among the two beam-splitters and the mirror; the procedure begins with the bonding of the optics to the metal supports, which were designed to allow for the automatic alignment procedure and to also be removed after the optics are permanently joined to the baseplate. The supports, visible in Figure 2.8 and 2.18, are glued to the optical components using the adhesive with the characteristics detailed in Figure 2.9, while the connection between the optics and the baseplate is to be achieved using a different type of glue (UHU Plus Endfest 300, Table B.4 and Figure 2.13). The different characteristics of the two adhesives with increasing temperature allow for the separation of the metal supports from the optical components using a local increase in temperature, which affects the Schnellfest at much lower temperatures than the Endfest. The metal supports also contain a slit between the heat cartridge and the upper portion, which hinders the heat transfer to the part that needs to be manipulated and therefore decreases the risk of injury.

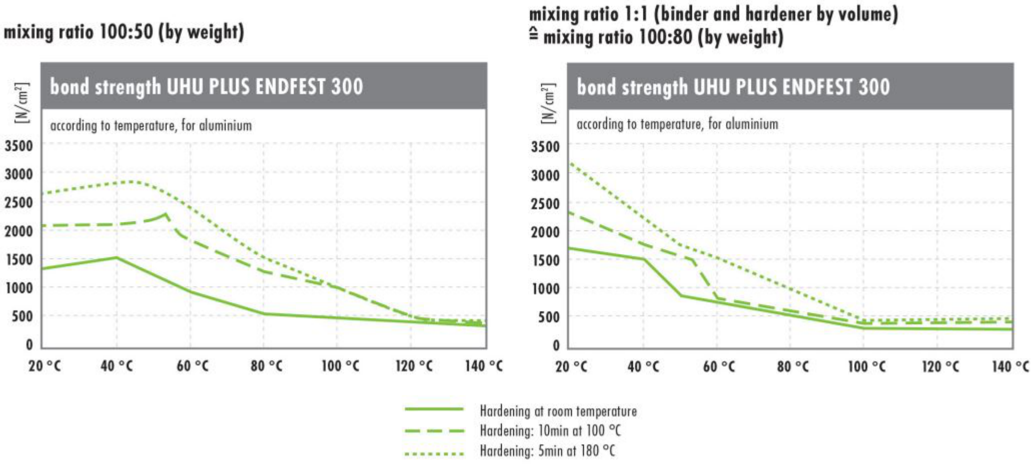

Figure 2.13: Bond strength of the UHU Plus Endfest epoxy glue as a function of temperature and mixing ratio [18]

For all optics, it is important to verify the actual position of the reflective coating; this can be achieved by a simple test with the laser beam. The orientation of the beamsplitter is fundamental to the correct operation of the interferometer; the position of the reflective coating for the left and right side is clearly visible in Figure 2.14, as the reflective coating is the part of the optical component where the incoming beams are split or recombined.

As can be seen from Figure 2.14, the information contained in the interference produced by the two beams is sent to a QPD, or a Quadrant PhotoDiode on the right side. Quadrant, or segmented, photodiodes consist of four active areas separated by a very narrow gap. The photodiode is aligned so that the laser spot falls on the intersection between the quadrants. By detection of the relative photocurrents produced by each segment, any deflection in the laser beam can be accurately measured. [19, 20]

With reference to Figure 2.15, the coordinates of the center of the beam can be calculated by

$$\begin{aligned} x_{position} &= k_x \cdot \tfrac{(V_A+V_D)-(V_B+V_C)}{V_A+V_B+V_C+V_D}, \\ y_{position} &= k_y \cdot \tfrac{(V_A+V_B)-(V_D+V_C)}{V_A+V_B+V_C+V_D}. \end{aligned} \tag{2.2}$$

The quadrant photodiode used in the present setup is a InGaAs photodetector; the data is extracted by connecting it to a PCB designed for this end. The light that reaches

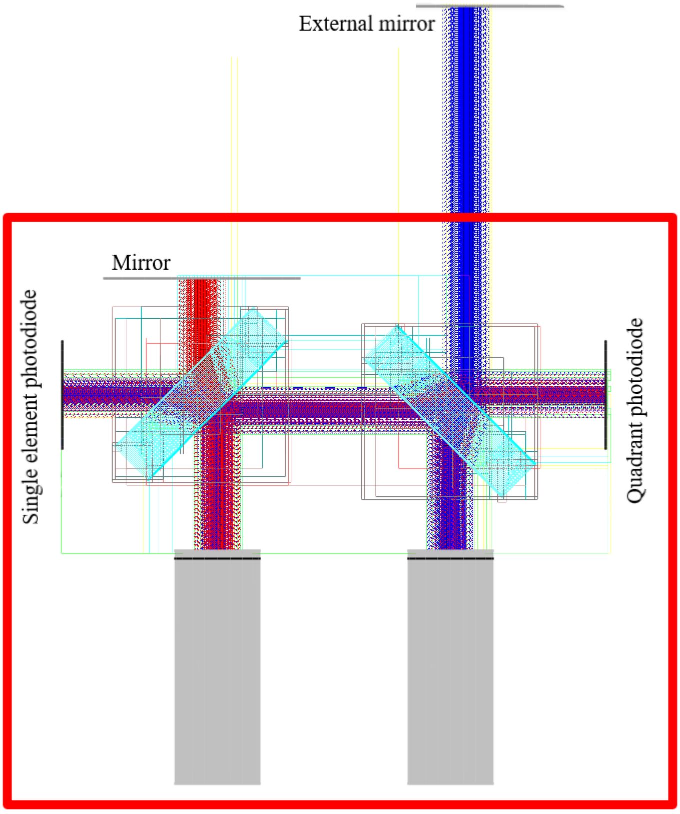

Figure 2.14: Detailed depiction of the expected behaviour of the beams inside the interferometer [22]. The blue (right) beam leaves the interferometer to a moving mirror, providing information about its position, while the red (left) beam is used as reference. The position of the reflective coating on the beamsplitters can be clearly noticed by the position of the incoming beams, and was used to define the correct procedure for the bonding of the metal supports.

each quadrant generates a certain number of hole-electron pairs, therefore generating a current that is proportional to the amount of light on the surface; the PCB employs operational amplifiers to convert the photocurrent to a voltage, which makes the calculations in the previous equation possible. A similar behaviour, albeit with loss of information due to the lack of the four quadrants, is expected from the single element photodiode soldered to another PCB mounted on the left side; this second photodetector is used to provide the differential measurement. Both printed circuit boards were soldered in all parts. The access to the collected data is possible thanks to the USB connection on the PCB that contains the QPD and a microcontroller.

A preliminary alignment of the components was performed manually; the results were

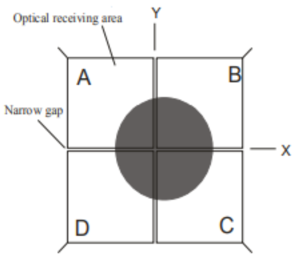

Figure 2.15: Principle of operation of a quadrant photodiode; when the beam is perfectly centered, the voltages on each quadrant are equal. When there is a deflection, the coordinates of the center of the beam can be calculated as a function of the voltage originating from each quadrant. [20]

satisfactory, since interference was achieved. This was verified by changing the beat frequency to 1 Hz and observing the pattern of the superimposed beams; if the laser was blinking with no fringes, then the alignment of the beamsplitters was good; if fringes were present on the diffraction pattern, the position of the beamsplitters could be adjusted to eliminate them. To optimize the alignment, however, the automatic system is needed. During this stage of the process, it was required to employ a mirror positioned outside of the baseplate.

In order to further better the alignment before launching the automatic optimization, it was necessary to verify whether the beam was correctly exiting the interferometer, meaning the height, position and angle of the beam were satisfactory for the subsequent positioning of the QPD. To achieve such improvement, it was necessary to edit the design of two of the constructed QPD mounts; they were cut to fit under the mirror mounts, and a ∅2 mm counterbore hole was cut. The presence of the hole, of a diameter comparable to the diameter of the beam itself, allows the formation of a diffraction pattern on the outside of the interferometer. Simulations were performed with different values of offset from the ideal position, and these patterns were used as reference in the comparison to the one measured (Figure 2.16); the adjustment achieved by acting on the available degrees of freedom had the goal to approach the perfect alignment. It is important to note that, in this phase, the lateral mounts were connected to the baseplate using countersunk screws, which aid in the alignment of the center of the hole to the center of the thread. However, when the alignment is completed and the construction of the interferometer is close to conclusion, the screws will be substituted with the cap screws required by design.

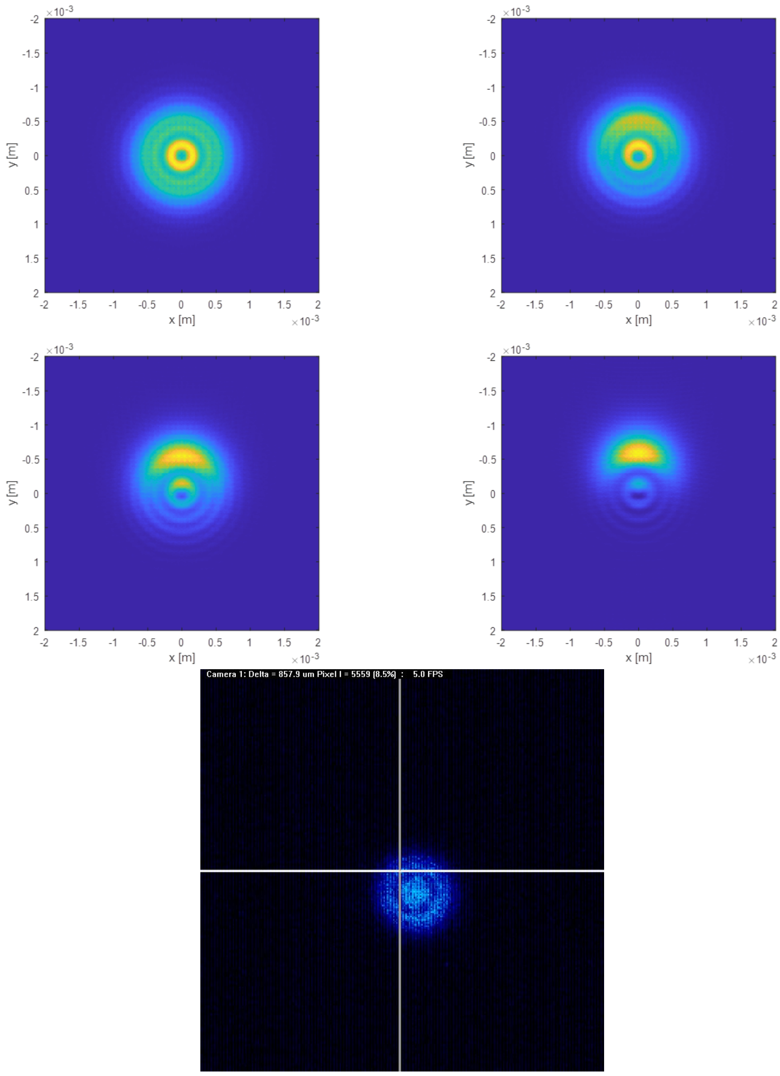

Figure 2.16: Simulation of the diffraction pattern from a ∅2 mm Gaussian beam clipped at a ∅2 mm hole and analyzed at a distance of 25 cm. From top left, the pictures show perfect alignment, 0.2 mm offset from the center, 0.5 mm offset from the center, 1 mm offset from the center [21]. During the alignment process, the diffraction pattern captured by the camera was compared to the simulation, to evaluate the direction and entity of the correction needed. The last image shows an example of such a measurement, from which it is possible to say that the alignment with the center of the hole is satisfactory.

The beamsplitter alignment procedure requires the activation of the steering mirror control loop; the light being emitted from the right fiber launcher hits the mirror, which performs a scan of the position of the beam and then rotates according to the measured parameters to achieve a backreflection of the beam that is coupled back into the right fiber launcher. In order to assess the successful completion of such control loop, a powermeter was added to the frequency generation setup (Figure 2.3 and 2.4), on the path of the beam originating from AOM #1 and being reflected by the following beamsplitter; the backreflection, coming back from the fiber launcher, is affected by some parasitic reflections that affect the reading on the powermeter. To reduce the amount of noise in these measurements, the beam path was enclosed in black cardboard. After the steering mirror loop has been activated, the position of the beam in respect to the aperture on the lateral mount is evaluated and, if need be, corrected by acting on the available degrees of freedom. The objective is to reach a satisfactory preliminary alignment before activating the more precise and accurate control loops.

Then, the position control loop and the angle control loop can be enabled; they receive data from the QPD on the position and relative angle of both beams, calculate the error, evaluate the number of steps necessary to reduce the error, and activate the piezo-steppers to actuate the movement; the angular resolution that is achieved by the steppers is considered to be 1.4 μrad. The correction can be performed after the adhesive has been applied, to perfect the alignment as the curing process continues. The QPD provides the raw data on the beam intensity in each quadrant to the phasemeter, which uses the microcontroller and the attached printed circuit to process the data (although partially) and returns the phase information which is used by the steering mirror program and its control loops and later on by the thrust balance software. The basis for the control loops is a phase-locked loop (PLL); it generates an output signal whose phase is related to the phase of an input signal, for example it compares the phase of a reference signal to that of an adjustable signal. In brief, in an analog PLL, a phase detector compares the input and the feedback signal, producing an error signal that is therefore proportional to the phase difference; the error signal is filtered using an application-specific low-pass filter, and then fed to a Voltage Controlled Oscillator to generate the output phase. In an unlocked state, the phase difference between the two signals is free to change; in the locked state, however, the phase difference must remain constant, and therefore the control loop is activated to correct the variations. Since the phase difference is constant, the frequency of the two signals is the same (since the integral of frequency is phase). A graphical representation of a PLL is shown in Figure 2.17. [28]

The PLL that is used by the microcontroller is an all-digital PLL; the principle is the same as the analog, but the phase detector, the filter and the oscillator are all digital. The Voltage Controlled Oscillator is replaced by a Numerically Controlled Oscillator.

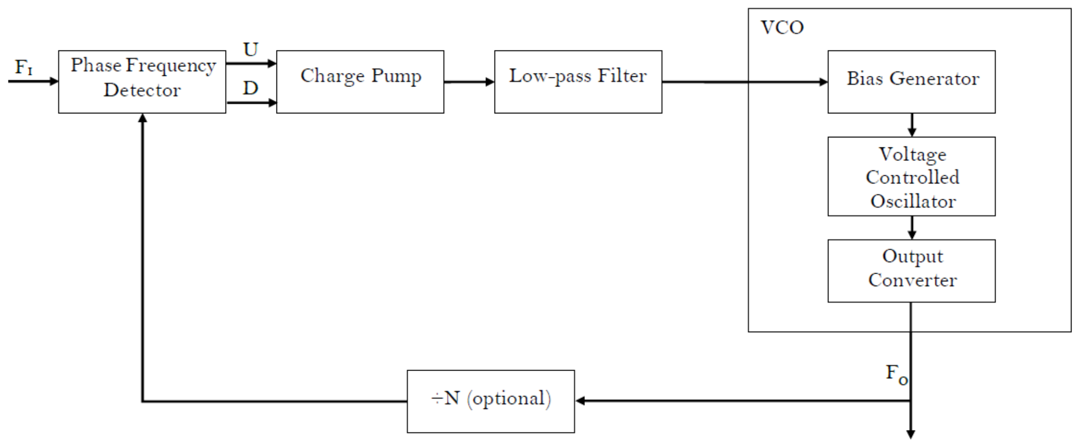

Figure 2.17: A phase-locked loop (PLL) generates an output signal whose phase is related to the phase of an input signal. A phase detector compares the input signal and the feedback signal, producing an error signal (proportional to the phase difference). The error signal is then filtered and fed to a Voltage Controlled Oscillator (in an analog PLL) to generate the output phase. Phase noise, which is related to the power of the noise of the PLL, is mostly influenced by the N counter value; N should be as small as possible to avoid multiplying the noise. In frequency generation, the N parameter is what allows the PLL to generate different frequencies. The all-digital PLL that is used by the microcontroller is similar in principle, but the components of the cycle are all digitally implemented; the VCO is replaced by a Numerically Controlled Oscillator. [28]

The control loops, both for position and angle, use a purely proportional controller, whose constants are given in input by the user. It has been noticed that the position control loop has a greater effect on the piezo-steppers in comparison to the angle control loop; therefore, the proportional constants were chosen so as to balance the two behaviours. The alignment program is designed to allow for both individual and joint alignment of the four variables; each variable's corresponding control loop is activated by the user, in response to the measurements that are displayed on the graphical interface. The graphical interface provides the following information to the user:

- position of each beam on the QPD

- status of the QPD (if locked, and the microcontroller is using the QPD data as a source for the PLL, $status = 7$; if the microcontroller is instead using the data from the single element photodiode for the PLL, as it does during the operating life, $status = 3$ if the loop is locked)

- AC amplitudes on the QPD (they represent the quantity of light that is hitting the QPD in each quadrant; for optimal alignment, they should be as close as possible, and they should attest around 75%)

- calculated error for position along the *x-axis* in mm

- calculated error for position along the *y-axis* in mm

- calculated error for angle along the *x-direction* in mrad

- calculated error for angle along the *y-direction* in mrad

- the beat frequency in Hz (it is useful in the event that the PLL is locked, but at a different frequency than it should)

The target values for the errors are summarized in Table 2.2. The position error can only be affected by the alignment of the beamsplitters, while the DWS error is also affected by the alignment of the mirror; because of this, initially the DWS error is accepted at a higher value and then improved upon afterwards. After the curing process, the beamsplitters produced a very satisfactory alignment.

Target values for the alignment process

	Position error	**DWS error**
For the integration of the beamsplitters	< 0.05 mm	< 0.05 mrad
For the integration of the mirror	-	< 0.01 mrad

Table 2.2: Target values for the alignment process; it is intended that the mirror alignment follows the beamsplitter alignment and gluing, and therefore the objective in this case is to improve the DWS error.

The removal of the metal mounts was achieved by connecting the heater cartridges to a power supply, and then using electrical power to generate the heat.

In order to complete the optical component integration, the mirror needed to be glued; by design, this involved the rotation of the baseplate, as seen in Figure 2.8, in a counter-clockwise direction so as to mount the metal support for the mirror on the left piezo-stepper structure. However, important criticalities were found with such an approach:

- the right beamsplitter would collide with the right mirror mount to reach the correct position
- one of the screws that controls the tilt of the optical components is lower on the left side, which creates difficulty during the phase of reinstallation of the optics after applying the glue.

Therefore, it was decided to instead rotate the baseplate clockwise, to protect the fragile beamsplitter already consolidated with the baseplate.

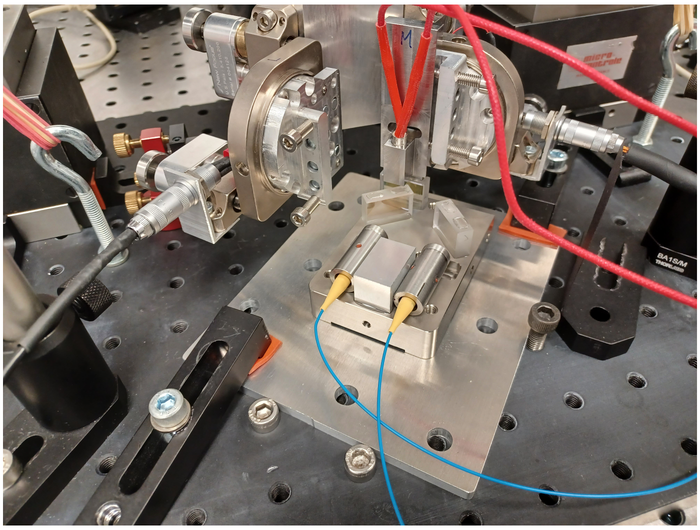

Figure 2.18: Detail of the modified setup for the mirror consolidation. This image also provides a more precise perspective on the process described up to this moment. [21]

For the alignment of the mirror, the steering mirror loop is not necessary; it is instead necessary to receive light on the photodetector. The chosen approach was to use the QPD, as the alignment program was conceived with the information provided by this sensor; in the completed interferometer, however, the left mount would host a second PCB with a photodiode. In order for the laser beams to reach the QPD, it was necessary to employ two additional mirrors, to account for the obstacles on a more direct beam path; the increased number of reflections that the beams underwent, however, caused the need for a variation in the sign of one of the proportional constants in the angle control loop (in the present case, two reflections were needed, and the constant for the angle along the *x-direction* needed to be multiplied by -1). Since the alignment of the mirror only affects the left beam, it is necessary to align the auxiliary mirrors so that the right beam is in the center of the photodetector; after this, the DWS control loops can be started.

The procedure for the final integration of the mirror follows the same steps as the beamsplitters, but the only control loops that are activated are the DWS control loops. The adhesive used between the mirror and the baseplate is UHU Plus Endfest, and between the mirror and the metal support is UHU Plus Schnellfest, to again be able to exploit the different thermal behaviours for the removal of the support.

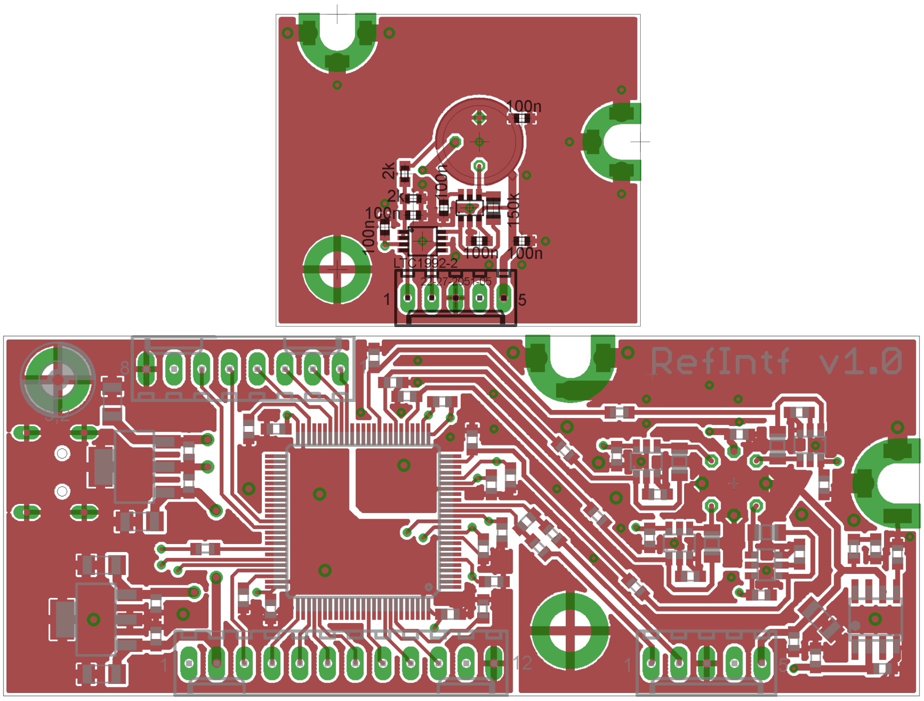

Figure 2.19: Schematics of the two PCBs, that allow for the differential reading with data from a single element photodiode and a quadrant photodiode. They are to be connected to each other using the five pins on the bottom side of each PCB: pin #3 is the ground connection, pins #1 and #2 are the signals and pins #4 and #5 are the voltages. It is also possible to visualise the correct orientation of the photodiode on the larger PCB. [21, 22, 26]

To complete the operating structure of the interferometer, it is still necessary to mount the PCBs containing the QPD and the PD. This is made possible by the lateral mounts; they provide three points of connection in which the alignment of the PCB can be perfected. Since the device needs to be used in a vacuum environment, it is necessary to modify the lateral mounts to include a path for the air to leave the interferometer, in particular in the portion of the mount that is in contact with the baseplate. To correctly align the two PCBs, it is important to maintain them as parallel as possible to the baseplate; then, the right beam is blocked and the two photodiodes are aligned using the information given by the alignment program and the interferometer testing program (see Section 2.4 and Appendix B), so that the DC amplitude values are maximum. When this happens, the right beam can be unblocked and aligned using the external mirror.

The two PCBs need to be connected in order to perform the differential measurement in the phase, so a connector needed to be constructed; with reference to Figure 2.19, pin #3 is the ground connection, pins #1 and #2 are the signals and pins #4 and #5 are the voltages, and they need to be connected to the corresponding pins on the other PCB. The cables were then weaved together and fed through the slits in the top portions of the lateral mounts. Before the connection could be completed, it was necessary to cut and sand part of the pins for the connector on the side of the PCBs fastened to the lateral mounts, since the contact with the metallic surface was causing a short-circuit.

After the connection was performed, it was necessary to modify the software interface so that the source for the data for the PLL was switched from the QPD to the PD. Such intervention allows for the interferometer to perform the differential measurement that is needed to evaluate the distance. In this new configuration, the *locked* status for the PCB is represented by the number 3.

2.4 Testing and characterization of the finished interferometer

Following the procedure of integration of the optical components to the supporting structure, the interferometer needed to be tested to demonstrate the capability of measuring

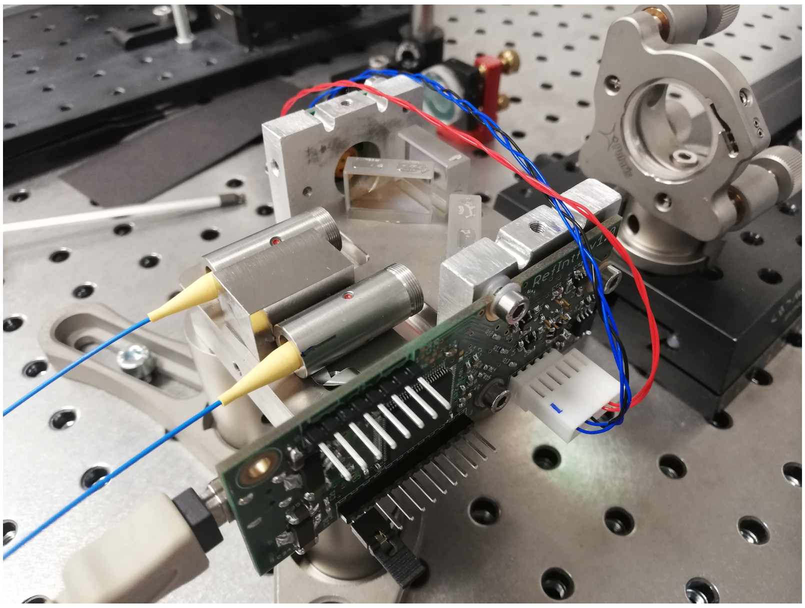

Figure 2.20: The complete interferometer, in the testing position. The external mirror can slide on a graduated track, mimicking the operating life and allowing for the verification of the data given in the user interface.

displacement and angle.

In order to simulate the behaviour of the interferometer during the functional life, an external mirror was mounted on a sliding structure; this allowed for the completion and testing of the software interface, to correctly display to the user the path length variation and the DWS measurements. Information about the user interface is provided in Appendix A and B.

The procedure for testing the interferometer was composed of the following actions:

- adjusting the external mirror to find the maximum of the beat signal power, making sure that no significant difference would arise between the four quadrants. Should this be the case, the corresponding PCB would need a slight adjustment, while making sure that the DWS signals are not too high and the power of the signal is strong;
- use the reset button for the DWS values;
- adjust the external mirror once again to bring the DWS measurement as close to

zero as possible;

- use the reset button for the path length;
- slowly slide the external mirror of a known distance in order to verify the correct acquisition of the data.

The preliminary testing of the interferometer was deemed successful, proving the capability to measure variable distances with acceptable precision and DWS up to 3 mrad in module. The complete characterization of the finished product, however, will need to be performed in the vacuum environment, as the air movement in the current setup introduced a significant source of noise. Nonetheless, a noise characterization was performed, with encouraging results visible in Figure B.4.

Another test was performed in order to determine the maximum velocity that could be tracked by the interferometer without losing the *locked* status; this test entailed changing the low-pass filter coefficient that was programmed on the micro-controller present on the PCB containing the QPD. The initial value for such a coefficient was 0.98, and the lock was lost at a beat frequency under 900 Hz; the advantage of this configuration was a reduction of the effect of noise, though the performance in terms of the velocity was not optimal. Results for the test are summarised in Table 2.3.

Value of the low pass filter coefficient	0.98	0.9	0.8
Beat frequency at which the lock is lost	900 Hz	5000 Hz	10000 Hz
Estimated maximum speed (beat frequency 30 kHz)		0.3 mm/s	0.5 mm/s

Table 2.3: Results for the maximum velocity test

2.4.1 Test in vacuum

In order to completely characterize the interferometer, it was necessary to perform a test in vacuum, to eliminate the noise from the movement of the air and to verify the alignment stability as the pressure decreases. To this end, the interferometer was connected to a small plate, on which a mirror was placed; the plate was then inserted in a small vacuum chamber to perform the test. The preliminary test needed to happen in this smaller chamber because the protective covers were not yet available, and it was deemed too risky for the optical components to be placed in the thruster testing chamber with no protective layer.

In the interest of obtaining the data from the device once inside the chamber, it is required to provide appropriate feedthroughs; these are assemblies whose main purpose is to carry substances or energy from the outside to the inside of a sealed vacuum chamber and vice versa. They are designed to avoid leakages under different grades of vacuum. The feedthroughs present on the available vacuum chambers have a DA-15 D-sub interface; therefore, the USB connection that was used outside the chamber needs to be modified to include this type of connection on both interfaces of the vacuum chamber. For the fibers, the employed feedthroughs were polarization maintaining, single mode vacuum flanges from Schäfter + Kirchhoff; since it is composed of a single fiber, it was necessary to use multiple fiber-to-fiber connectors to achieve the transfer of light to the fiber launchers. The connectors typically reduce the power transmitted to the receiving fiber, therefore some losses were expected.

The first important result derived from the vacuum test was the confirmation of the stability of the alignment, in other words the demonstration that the decreasing pressure did not cause a shift in the position and angle of the optical components. An estimation of the contrast (indication of the quality of the alignment) was performed using the ratio between the AC and DC values; before the chamber was closed, the contrast could be gauged to be around 93%. After the vacuum chamber reached the lower pressure condition, the contrast remained acceptable at approximately 88%; moreover, the PLL lock stability was satisfactory.

During the first measurements, it was apparent that some issues were present in the experimental setup, as the measured performance in vacuum was very poor in comparison to the previous tests; therefore, the setup was analysed to determine the cause of such decline in the capabilities. After excluding the software (though, at the time of this test, some issues were present in the software that were later identified and corrected), it was decided to perform an additional measurement to verify that the issue was not determined by the interferometer itself; this assessment entailed the substitution of the beat frequency with an amplitude modulation with a corresponding frequency, so that one beam could be blocked and the only noise that would be measured would be from the electronics. The results of such a test were positive, since the noise level remained below 10 $\mathrm{pm}/\sqrt{\mathrm{Hz}}$; moreover, it was highlighted that the behaviour of the two sets of fibers used was extremely different (2 orders of magnitude in the path length), supporting the hypothesis that the optical fibers were the reason for the diminished performance. The complete results for this test are depicted in Figures 2.21 and B.5.

Multiple such tests were performed, increasing the duration to more completely characterise the device. In Figure 2.22 it is possible to view the results derived from an overnight measurement (around 17 hours). In both tests it is possible to notice the absence of any drift in the pathlength measurement, which is a positive sign that the device is correctly operating; moreover, the noise level of 0.1 $\mathrm{nm}/\sqrt{\mathrm{Hz}}$ at a frequency of 1 mHz is acceptable for the interferometer planned applications.

2.5 Design of the interferometer cover

In Figure 2.2, it is possible to observe the final look of the interferometer; however, it is necessary to provide protection against damages and impurities so that the optical components maintain a correct behaviour. For this reason, a cover needs to be added to the final assembly. During the design phase of the interferometer device, the proposed approach was to have a front panel, connected both to the baseplate and the lateral QPD mounts, and a separate cover for the remaining parts, which would also be connected to the QPD mounts. Such a proposal can be seen in Figure 2.23.

However, a revision of the design brought about the modification of the original idea;

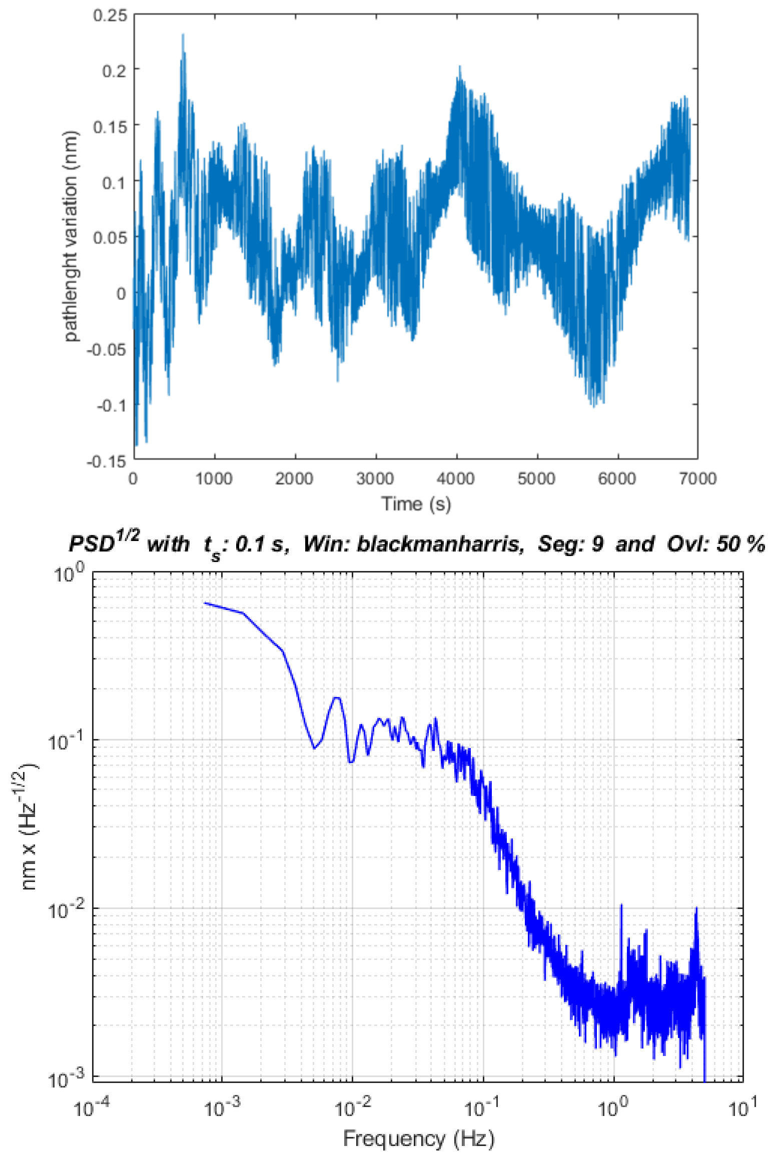

Figure 2.21: Results from the measurement in vacuum using the amplitude modulation. The frequency was set to 20 kHz, and the depth of the sinusoidal signal to 100%; the contrast in this case is close to 97% (thanks to the amplitude modulation). The results are encouraging as the noise from the electronics is below 10 pm/$\sqrt{\text{Hz}}$ even at higher frequencies. The results from the DWS measurement can be found in Figure B.5.

in its stead, it was proposed to incorporate both sections previously described into one single piece, and to change the chosen material from aluminium to stainless steel. The new design would have some advantages:

- having one single piece instead of two would reduce the risk for misalignments at least at the original interfaces, and would also mean a more stable connection especially

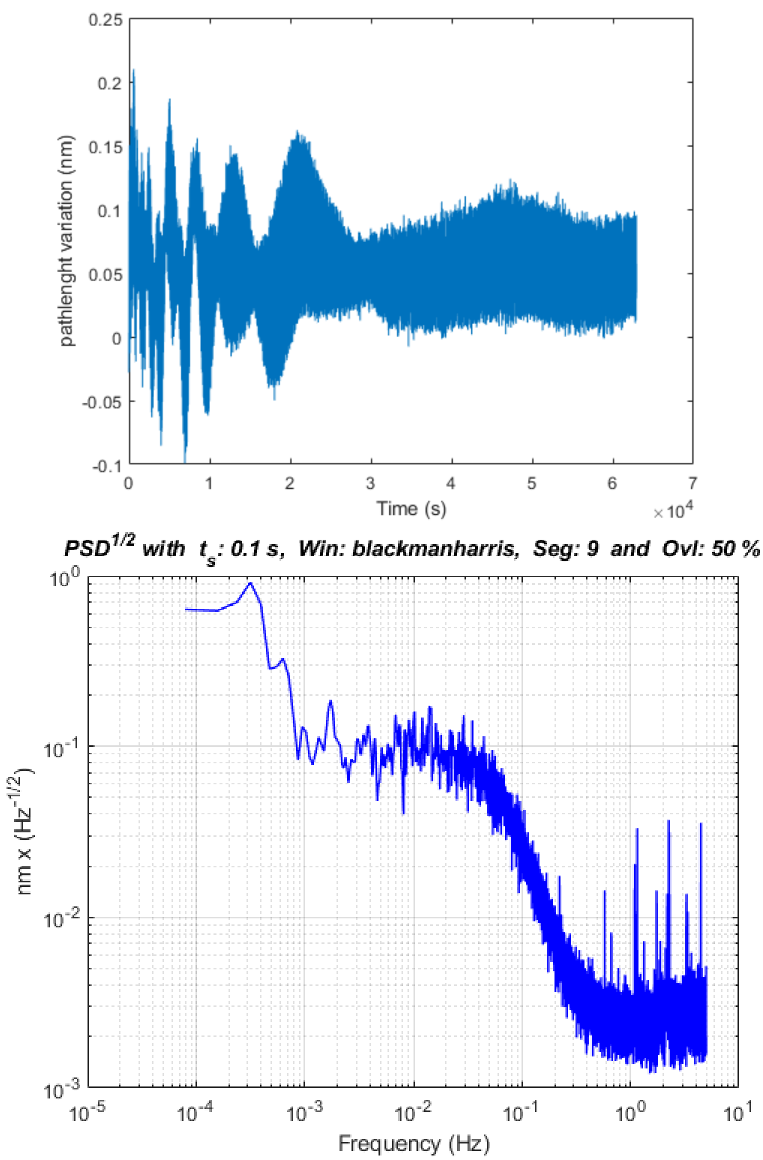

Figure 2.22: Results from the overnight measurement in vacuum using the amplitude modulation. The frequency was set to 20 kHz, and the depth of the sinusoidal signal to 100%; the contrast in this case is close to 97% (thanks to the amplitude modulation). It is encouraging to see that there is no drift in the pathlength measurement, and the noise level of 0.1 nm/$\sqrt{\text{Hz}}$ at a frequency of 1 mHz is acceptable for the interferometer planned applications. The results from the DWS measurement can be found in Figure B.6.

for the upper portion of the cover

- the one piece solution would be more open to multiple options of manufacturing (originally the top cover was supposed to be made from sheet metal, while the single piece cover could be obtained both through milling and bending of the sheet metal)

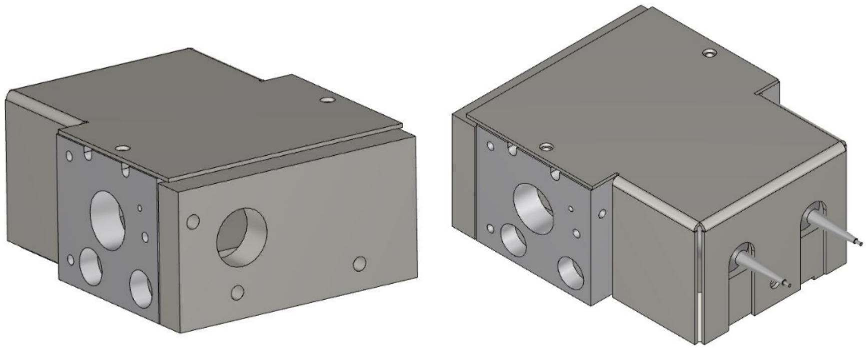

Figure 2.23: Initial proposal for the cover of the interferometer; it is composed of two pieces, one of which is produced via bending of sheet metal. The connections are provided by screws in the front of the baseplate (for the front panel) and on the side mounts (for the upper cover). [21, 22]

- the change in material is deemed important as the interferometer needs to survive in an aggressive environment, and stainless steel is more resistant to the expected corrosion than aluminium is; however, using stainless steel would prove more complex if it was decided to produce the cover using sheet metal

Before proceeding with the construction of the final covers, a prototype was 3D-printed and verified against the already existing hardware to, if needed, adapt the design.

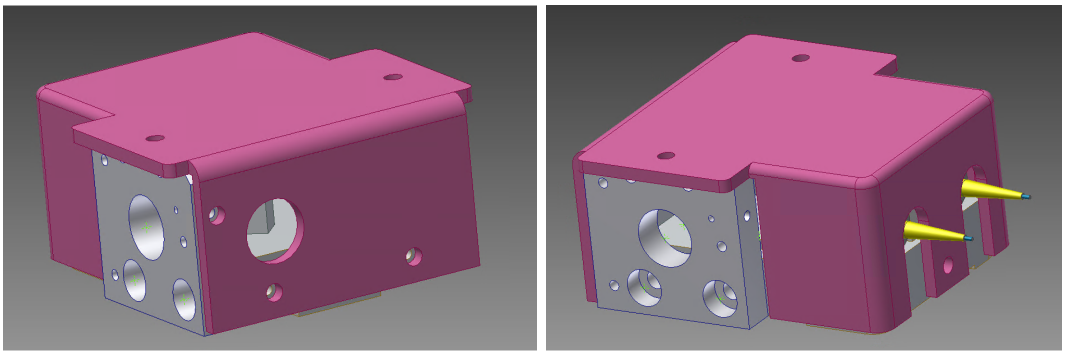

Figure 2.24: New design for the interferometer cover. The basic configuration is maintained, but the design is modified to accommodate the new manufacturing method (milling). The portion that connects to the lateral mounts is extended to better cover the PCBs. The pink color is used to simply highlight the new design.

As can be seen in Figure 2.24, the new design is similar to the original, but with a few adaptations to make the manufacturing process possible. Moreover, the portion that connects to the lateral mounts was slightly extended to provide a layer of additional protection to the PCB components.

The specifications for manufacturing are shown in Table B.5.

Chapter 3

Thrust balance update, integration and testing

The characterization of any thruster, inevitably, contains information about its thrust generation capabilities. When it comes to micro-Newton thrusters, their applications often impose very strict requirements, which in turn generate particular requirements for the measurement facilities. For instance, the micro-Newton thruster facility at Airbus in Friedrichshafen was designed on the requirements derived from missions such as LISA (Laser Interferometer Space Antenna, [25]), which can be summarized in Figure 3.1.

The thruster diagnostic facility is composed of a custom built vacuum chamber, a plume diagnostic setup and a micro-Newton thrust balance. For the purposes of the present study, the description of the operating principle and of the architecture of the thrust balance is fundamental; more information about the remaining devices that constitute the test facility is available in the published work from Dr. Hey [24].

Concerning the thrust balance, the thrust range and the thrust noise requirements of LISA and other similar missions imposed the requirements contained in Table 3.1. [24]

In principle, the architecture of the thrust balance is quite simple: it is composed of two identical pendulums, a reference pendulum and a measurement pendulum. The thruster is mounted on the measurement pendulum, while the reference pendulum is fitted with a

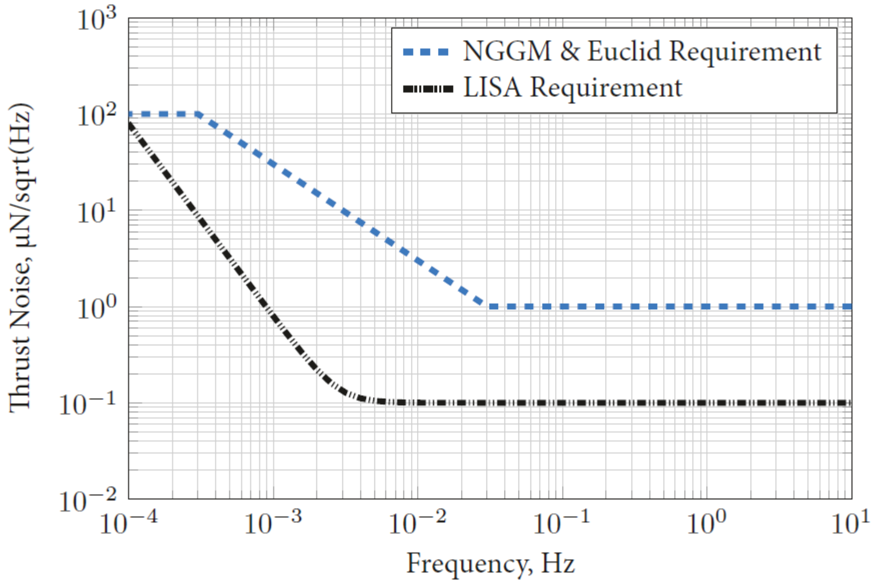

Figure 3.1: Summary of the thrust noise requirements of LISA plotted as a function of frequency. In the diagram, requirements for other missions that need highly precise AOCS systems are shown. [24]

Thrust range	0-2500 µN
Measurement bandwidth	10 Hz to $1 \cdot 10^{-4}$ Hz
Thrust noise	$< 0.1\ \mu\text{N}/\sqrt{\text{Hz}} \cdot \sqrt{1 + (\frac{10\ \text{MHz}}{f})^4}$
Thrust resolution	< 0.1 µN
Max. thruster weight	6 kg

Table 3.1: Requirements for the thruster diagnostic facility [24]

model of the thruster; when the thruster fires, the deflection caused on the measurement pendulum is determined using a heterodyne laser interferometer, as is the position of the reference pendulum. The thrust measurement is given by multiplying the difference between the translations with the sensitivity results.

This architecture is particularly precise thanks to its symmetry, mechanical, optical and electrical; the differential translation measurement, combined with the symmetry of the setup, allows for the suppression of multiple noise sources and therefore the achievement of the wanted micro-Newton thrust measurements, with the possibility to extend into the sub-micro-Newton regime. Moreover, the current balance is compliant with the LISA thrust noise requirements. [24]

The presented thrust balance is able to operate in two different modes, *open loop* or

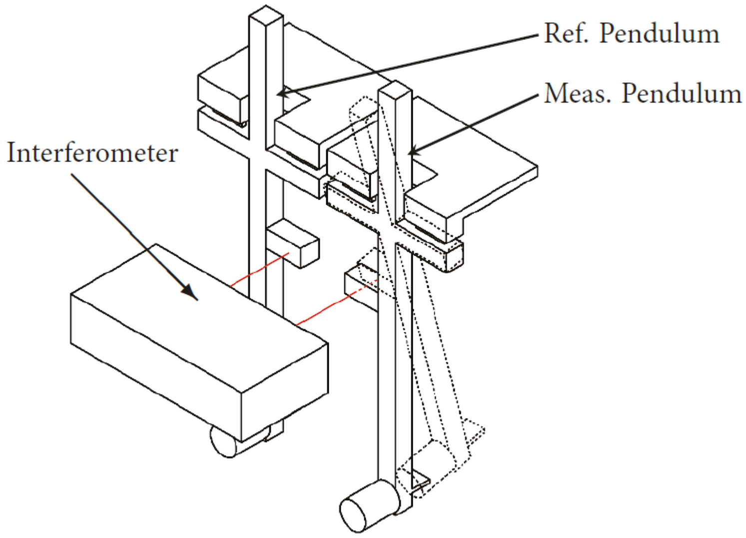

Figure 3.2: Principle of operation of the double pendulum balance. The laser interferometer evaluates the differential translation of two identical and symmetric pendulums, one of which is fitted with the thruster to be characterized. It is the very symmetry of the setup that allows for the achievement of the requested range of thrust measurements, since it is able to suppress noise from a variety of sources; for instance, thermal noise would not be measured by this setup, as it is reasonable to assume that both pendulums would be affected in the same way and therefore this noise would be eliminated by the differential measurement. [24]

closed loop; in open loop, the measurement pendulum is free to oscillate, and therefore the thrust is derived directly from the differential translation measurement. In closed loop, instead, an actuator prevents the pendulum from swinging, applying a force that is equal and opposite to the thrust. The open loop mode is used primarily for the thrust noise characterization, while the closed loop allows to measure more precise absolute values of thrust. [24]

The thrust balance is also able to provide the measurement of the deflection between the reference mirror and the measurement beam; this constitutes an additional measurement mode, called *DWS measurement*. The QPD measures the phase in four points over the beam cross section; then, a comparison is performed between two of such measurements, and therefore the QPD is able to provide information about the relative tilt between the mirror and the beam in two directions.

It is important to notice that the absolute measurement range of the interferometer is represented by half of the chosen operational wavelength; therefore, in this application,

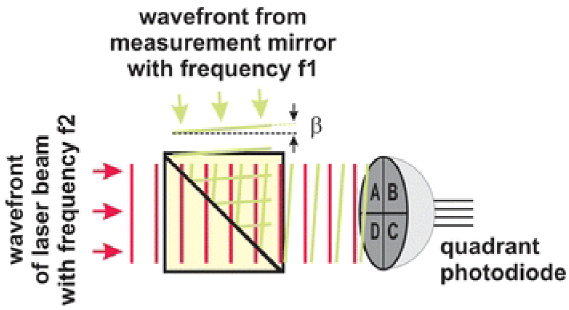

Figure 3.3: Illustration of the principle of measurement of DWS. As can be seen, the phase difference is easily measured by the QPD, and a comparison between the photocurrent of A, B, C and D is performed in order to determine the angle in the horizontal and vertical directions. [27]

the absolute range is equal to 532 nm. The limiting factor on the maximum measurement range is the quality of the superimposition of the laser beams; when the pendulum is deflected, so is the mirror that is attached to it, and therefore the beam might not be back-reflected into itself perfectly anymore. While the translation measurement is less affected by such limitation, the DWS measurement is non linear if the contrast, which describes the quality of the superimposition, is smaller than 50%. [24]

It is also important to mention that the vacuum chamber in the micro-Newton thruster facility in Friedrichshafen is used to test thrusters that employ a variety of propellants, including iodine; the aggressive environment created inside the chamber by this element is a primary concern when designing components and devices that need to operate inside the chamber. For instance, it is mainly for this reason that it was decided to manufacture the cover for the interferometer device using stainless steel instead of aluminium, namely to reduce the residuals and the dust created during the interaction between the iodine and the material constituting the cover and to avoid them falling on the optical components when the cover is removed.

3.1 Current architecture

As can be seen from Figure 3.4, the current architecture of the thrust balance consists of the two pendulums, the interferometer setup and the support structure. In particular, the support structure is composed of modular Item profiles, which create a more eas-

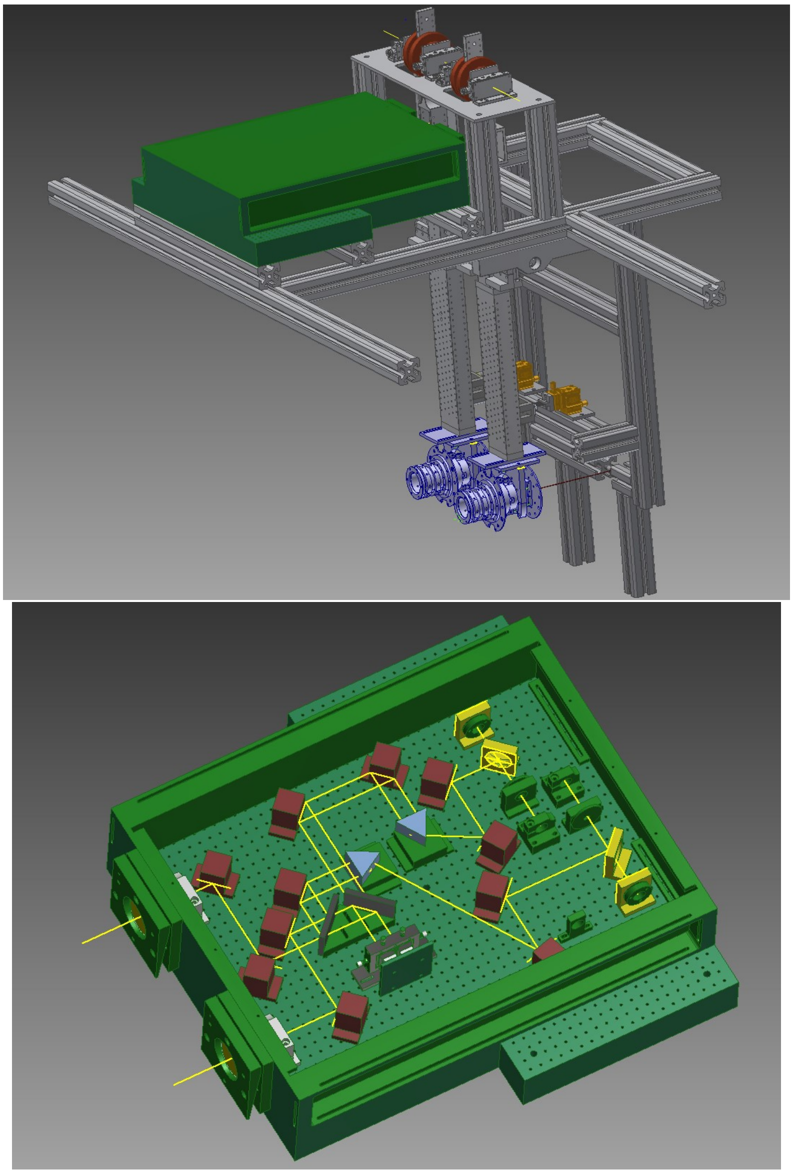

Figure 3.4: A CAD representation of the current thrust balance setup, including the interferometer that needs to be updated; the operating principle is the same as the new interferometer, but the architecture is vastly different. In particular, with the new design, the number of potential misalignment causes is reduced, since the optical components are consolidated to the same baseplate using an adhesive; in the current setup, instead, the optics are each mounted to a different support, which in some cases has created problems during measurement campaigns. [23]

ily adaptable architecture; this feature is particularly important for the purposes of the present work, as the modularity of the profiles was used to simplify the final design. In the detailed image of the interferometer that was currently being used, similarities with the new design can be noticed: the beam enters through fiber launchers, and is split to generate the measurement and reference beams. A Polarising Beam Splitter (PBS) is used when needed to obtain the correct s-polarization. The beams are then superimposed in order to create the heterodyne frequency and one QPD per beam is used to transfer the information to an electrical signal. When comparing the current interferometer with the new one, it is immediate to notice a few key differences:

- firstly, the dimensions: the new interferometer is made of two identical units, measuring around 80x70x40 mm, while the current interferometer box contains equivalent, but larger, optical components and therefore has a larger volume;
- secondly, the optical components are glued to the baseplate of the new interferometer, and therefore are more stable than the ones contained in the current version, which are instead mounted on supports and are more susceptible to misalignment problems;
- thirdly, the new interferometer setup will require four optical fibers in input to the interferometer box, while at this time only two fiber launchers are necessary; this causes the need for fiber splitters to be integrated in the design and the assembly process;
- finally, the materials used are different; while the vast majority of the current interferometer is constituted by aluminium, the baseplate and spacer on the new product are made from titanium, and the designed cover was made with stainless steel. The different materials might be beneficial during operations since the iodine environment is more intense on aluminium than on titanium or stainless steel.

The modifications made to the architecture will allow for a better working life for the thrust balance, as fewer adjustments would be needed; it is beneficial to achieve this goal especially due to the difficulty posed by the position of the adjustment tools inside the chamber.

At present, interferometer technology used inside the Airbus Defence and Space vacuum chamber has a demonstrated resolution of 5 pm in a bandwidth from 1 Hz to 10^{-2} Hz [24]. More characteristics of the current thrust balance setup are summarized in Table

Parameter	Specific Value
Estimated pendulum eigenfrequency	0.811 Hz
Derived balance sensitivity	0.022 µN/mm
Resolution of the interferometer technology	5 pm in 1 Hz to 10^{-2} Hz bandwidth
Theoretical thrust balance resolution (1 Hz to 10^{-2} Hz and with a targeted spring rate of 0.02 µN/mm)	0.1 nN

Table 3.2: Characteristics of the thrust balance before the modification of the interferometer setup. [24]

3.2.

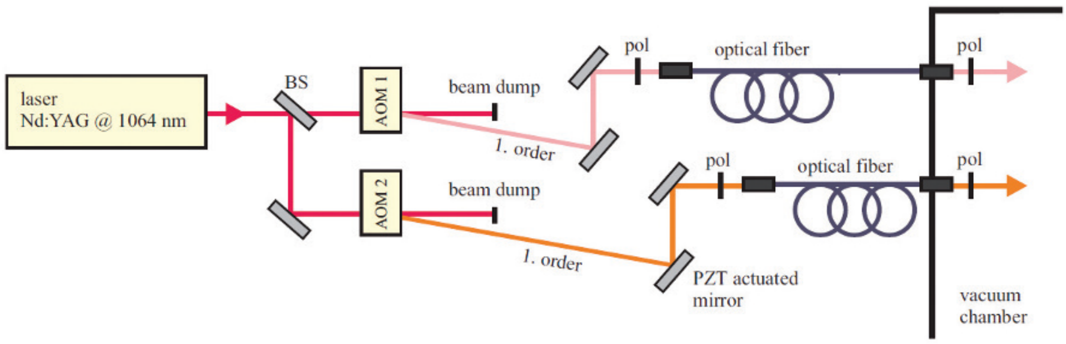

Figure 3.5: Picture of the laser interferometer setup inside the vacuum chamber, and sketch of the frequency generation setup outside the chamber. After being coupled into the fibers, the beams are launched from the fiber couplers and split to generate the measurement and reference beam (Meas. B. and Ref. B.). They leave the interferometer to be backreflected from the mirrors on the pendulum arms; the backreflected beams are again split and then superimposed on the QPDs, to translate the phase information into an electrical signal. [24]

3.2 Update of the interferometer setup

In order to design the integration of the new devices into the existing structure, it was necessary to employ the CAD software tools available; the complete design for both the interferometer device and the thrust balance structure was analysed and changes were proposed. The interferometer to be substituted was enclosed in a box; however, it was soon apparent that such a cover could not be repurposed for the new setup, as there was a conflict in the position of the apertures through which the laser beams left the interferometer. Moreover, the current architecture of the Item profiles did not allow for the achievement of the correct height for the beams to hit the mirrors on the pendulums.

For these reasons, it was decided to employ an OTS breadboard, on which to mount the interferometer baseplates, and that would be mounted to the supporting structure using appropriately sized spacers. For the spacers, it was decided to use the Item profiles already available in the laboratory, and to cut them to the correct size; this would limit the amount of components that needed to be ordered, and also maintain the modularity of the overall structure.

To connect the interferometers themselves to the breadboard, more than one solution was proposed; initially, it was suggested to drill appropriately placed holes in the breadboard itself, and to then use these holes to connect the interferometers to the breadboard from the three M4 threads on each baseplate. However, this solution was discarded due to the presence of connections hanging from the bottom of the breadboard; it is preferable for the design to avoid the possibility of pieces falling from above.

Therefore, it was decided to instead use tailor-made connections to provide a shared interface between the interferometer baseplate and the breadboard itself; this way, all parts would be secure and on the top side of the breadboard. Moreover, the design of such connections would provide much more freedom to adjust the position of each device as needed. In Figure 3.6, the connection is shown; the countersunk hole allows for the use of a screw whose head is then covered, and therefore the connection can be placed flat on the breadboard surface. The available material had a thickness of 5 mm, and therefore the design for the whole connecting structure would need to be adjusted to this offset.

For what concerns the connections to the supporting structure, multiple proposals were made; most of them, however, entailed the production or the commission of custom-made pieces, which would increase the costs and the difficulty of the setup integration. For these reasons, it was decided to use Item profiles, of the same type that already constituted the majority of the support structure, and cut them to size. This approach is beneficial since the modularity of the structure is somewhat preserved, and the needed materials were already available in the laboratory.

In order to connect them to the breadboard, it would need to undergo small modifications; in particular, since it was deemed more appropriate to use three points of contact, three additional holes need to be made in specific portions of the breadboard, in order to

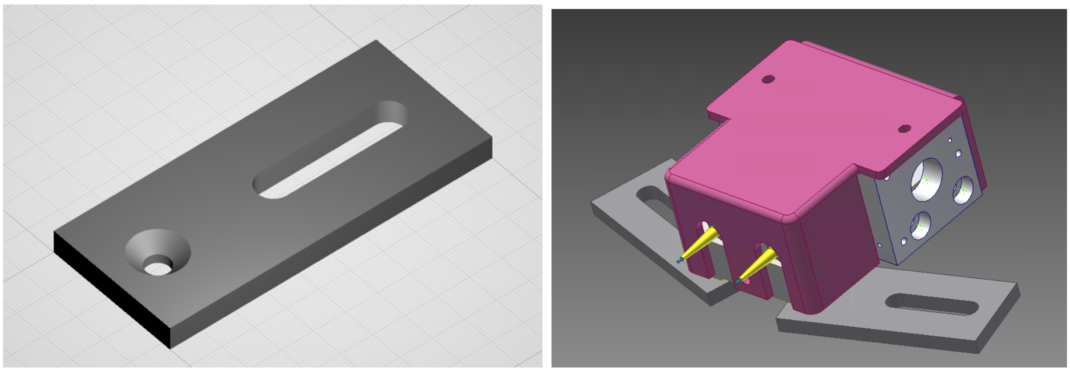

Figure 3.6: 3D image of the connection used to bind the interferometer to the breadboard (bottom view). The connection has a countersunk hole (∅5mm) that allows for the insertion of the M4 screw that then connects to the baseplate, and a bigger ∅7mm hole that can accomodate in many positions the M6 screw that is required by the breadboard threads. In the second image, it is shown how the connections can be used to provide different solutions to join the interferometer to the breadboard.

insert the screws that contribute to the connection. This would provide a sufficient number of constraints to the degrees of freedom, but without overly complicating the installation process.

As it was already mentioned, the vacuum chamber is used to test thrusters that employ a variety of different fuels, and in particular the research is focused on iodine. The interest in iodine as a spacecraft fuel is justified by its many advantages:

- since its density is four times the density of xenon, iodine provides a higher total impulse per volume of propellant;
- it can be stored at ambient temperature and pressure, and therefore does not require cryogenic infrastructure;
- it is less expensive than other propellants to procure (i.e., just 10% of the procurement cost of xenon);
- it can be stored at the solid state, therefore greatly limiting the transportation issues that arise with pressurized tanks; the propulsive subsystem can be shipped to the launch site completely assembled and ready for operation;
- it has been demonstrated that iodine is capable of performing similarly to xenon, at

least in gridded-ion and Hall-effect thrusters. [29]

Naturally, the use of iodine poses some obstacles:

- the operating temperature of the system needs to be maintained at around 100 °C, to contrast the tendency of the propellant to condense along the fluidic line;
- the selection of the materials needs to take into consideration the chemically aggressive nature of iodine, to avoid corrosion;
- there is still little data available on the interaction between the iodine plasma plume and the rest of the spacecraft, posing a risk for the operational lifetime of the most delicate parts (i.e. solar arrays and optics). [29]

It is the corrosive nature of iodine that most impacts the present work; to further protect the interferometer devices, the PCBs and the various connections, it was necessary to provide an additional cover. The design for this component is quite simple, since its only function is to enclose the small interferometers and their cables. It was decided to form it using sheet metal techniques applied to aluminium; this is justified by the higher ease of manufacturing and by the fact that this cover is not the protection layer closest to the optics.

The cover was designed to be able to connect to the breadboard in multiple places, to provide more flexibility during the installation and potential removals. Moreover, it allows for the addition of four supports, in the four corners of the breadboard, to integrate a further, but optional, thermal protection system. This would be constituted by a simple aluminium plate, which would provide an interruption in the thermal circuit inside the chamber; the heat flow, generated by the difference in temperature between the firing thruster and the vacuum chamber walls, would be interrupted by the aluminium plate and therefore the impact on the interferometers would be reduced.

3.2.1 Development of the software interface

For the acquisition of data, it was necessary to provide a software interface which reads, manipulates and stores the data. One simple program had already been created, to verify

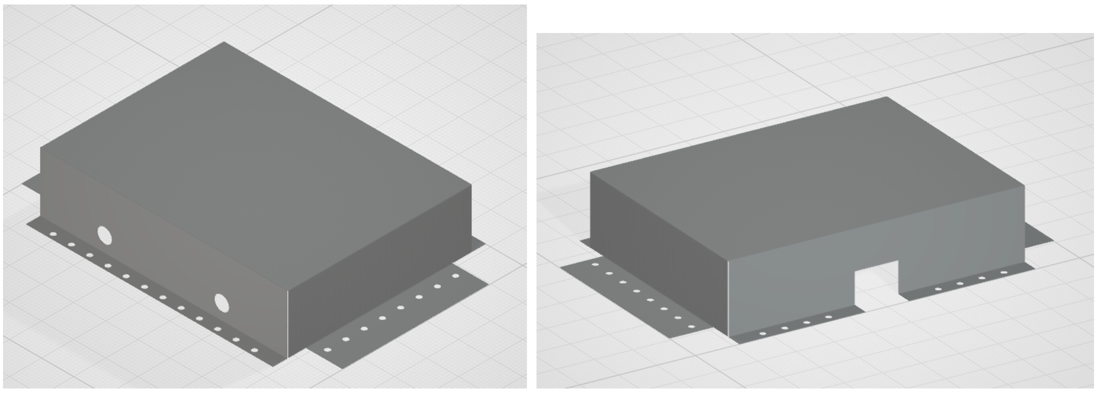

Figure 3.7: 3D view of the designed cover for the protection of the interferometers against the aggressive vacuum chamber environment. It can be noticed that the cover presents many options when it comes to the connections to the breadboard, to facilitate the installation. To minimize the number of apertures, all cables need to be fed through an opening on the back side.

that the interferometer was functioning correctly. However, in the workstation present in the thruster development laboratory, most of the interfaces use a different kind of programming language. Therefore it was decided to also design the software interface in such a language.

Since the LabView programming language allows for it, it was decided to implement most of the functions in a separate C++ file, and to then connect this file to the main window code written in LabView. The C++ file is compiled to create a Dynamic Link Library (DLL), whose functions can then be called by specific nodes in the LabView code. The program is able to identify the devices connected to the computer, connect them using the serial number (this particular function is very useful to not mix up the devices and therefore the measurements), read data from them and display the data to the user. It is also able to manipulate the data as needed, to convert the raw information into a more refined and useful output.

Concerning the display of data, the main window is composed of many indicators; the first available window gives the calculated values for the path length of the laser beam and the DWS measurements for both the reference and the measurement interferometers. It also contains the reset functions, so that the values of the measurements can be taken from a particular point in time. Additional windows allow to track the AC and DC power on each QPD, the lock status and the frequency. Moreover, a number of windows are dedicated to graphical depictions of the path length of each interferometer, the differential path length and the DWS measurements for each device.

Finally, the data is saved to a file, in order to access it after the measurement is completed; each file is marked with the date and time of acquisition. This makes it possible to trace the diagrams such as the ones in Figure 2.22 using a Matlab script.

To expand upon the architecture of the LabView interface, the following paragraphs will contain a short description of the operational behaviour of the code.

The first thing to be noticed is that the code is inscribed in a time-dependent frame; the content of each frame is executed and only when every instruction is complete the code moves on to the following frame. In this case, the order is as follows:

1. Reinitialization: the values of the variables are brought back to the default value

2. Get device list: a function is called using the function call node to enumerate the available devices connected to the computer

3. Connect devices: the code calls the functions that connect each device using the serial number

4. Read and display data: this step is constituted by a *while* loop, that runs until the user pushes the stop button on the main window. The loop starts if at least one of the devices is connected and breaks after the first iteration if not

    - the "Read Data" sub-VI is called, and it gives in output all the information that is required; most of it does not need any processing, so it is directly connected to the indicators on the user interface. After performing a number of measurements, it was apparent that the file size would not be sustainable; therefore, a for-loop was added within the sub-VI to reduce the sampling frequency (from 60 to 10 Hz; what is given in output is the average of the 6 values that were read within the for-loop)

    - the "phase" vector is instead given in input to a call function node so that it can be unwrapped and converted into cycles; another input/output of this function is the cycle counter, which needs to be saved from one iteration to the next

- once the phase is converted, the average path length is determined by calculating the average of all 4 values and multiplying it by the length of an half-cycle, which in this case is $1064/2 = 532$ nm; this calculation provides the measured distance between the interferometer and the external mirror (and not the two-way distance traveled by the light)
- the "Reset Path Length" and "Reset DWS" sub-VIs are then called; they contain the offsets that are used to perform the resets, and they are kept in memory for use in the following iteration. The resets allow for the user to start the measurement from a known point; they affect both devices at the same time so, when the "Reset Path Length" button is pressed, both the measurement and the reference interferometer will show a value close to zero as the new path length
- what can be directly displayed is connected to the indicators, while the rest is given as input to another sub-VI, which manipulates the data in order to then trace the real-time graphs for path length and DWS
- finally, the program generates a binary file in the chosen folder, and marks it with the date and time when the measurement was started; this allows for data from the same measurement to be saved to the same file, and at the same time it avoids overwriting data accidentally. Saving the data in a new file allows for the user to perform more accurate studies using more specialized external software.

5. Disconnect devices: the user has pushed the "stop" button; the functions to disconnect each device are called and the binary file is closed.

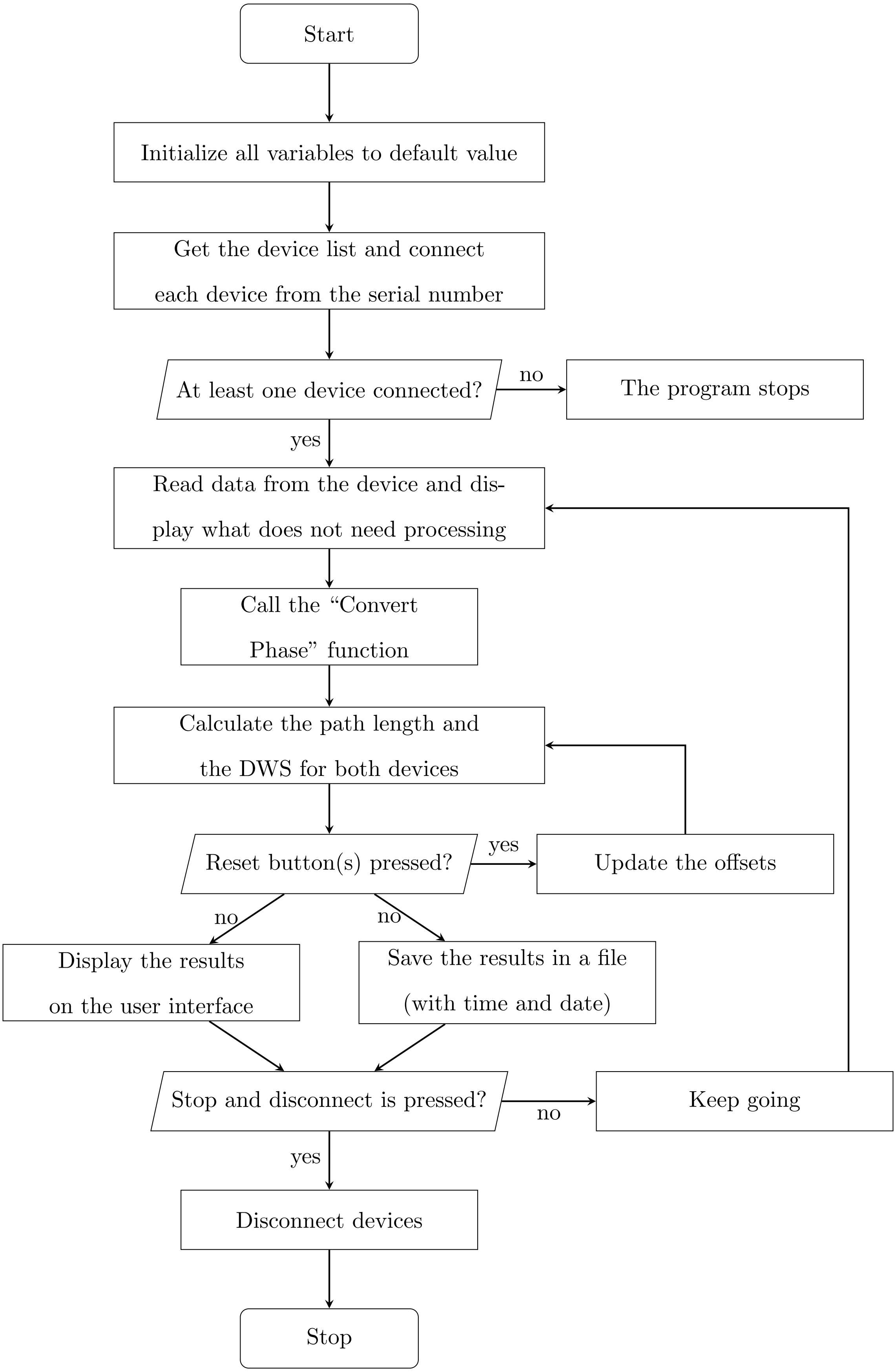
Start
Initialize all variables to default value
Get the device list and connect each device from the serial number
At least one device connected?
no
The program stops
yes
Read data from the device and display what does not need processing
Call the "Convert Phase" function
Calculate the path length and the DWS for both devices
Reset button(s) pressed?
yes
Update the offsets
no
no
Display the results on the user interface
Save the results in a file (with time and date)
Stop and disconnect is pressed?
no
Keep going
yes
Disconnect devices
Stop

3.3 Characterization of the updated thrust balance

To perform the preliminary tests to demonstrate the correct operation of the setup, the interferometers need to be mounted on the OTS breadboard; to simulate the presence of the pendulums, two external mirrors are also mounted in front of the devices, at a distance comparable to the actual operating distance.

In order to provide the correct laser frequency to both interferometers, and only having two fibers in output of the frequency generation setup, it was necessary to employ two fiber couplers (taps); fiber couplers (taps) allow for a single fiber input to be split into two outputs, with a particular ratio (in the present case, 50:50). The use of such devices allows for the corresponding fiber launchers to be fed the same laser beam, and therefore maintain their frequency as close as possible. One fiber tap would provide the laser beam to both left fiber launchers, and another one to both right launchers; the single end of each tap was mounted so that the insertion and removal of the input fibers would be as simple as possible.

In Figure 3.9, it is possible to see the proposed disposition of the interferometer devices onto the breadboard; the devices are positioned to be as close as possible to the mirrors on the pendulums, to minimise the operational path length, but with enough space to fit the external cover. The space on the backside of the two devices is used to distribute and consolidate the optical fibers and the USB connections.

For the optical fibers, the proposed solution is a cylindrical structure inside which the fibers can be looped and secured; this allows for the fibers to be protected from thermal stress derived from the USB connections and from possible mechanical stress. For the USB connection, a USB hub was deemed necessary to house the two cables connected to the devices, in order to only have one cable attached to the feedthroughs. The USB cables inside the breadboard were cut to an appropriate size, to minimise the space occupied by the connections.

Figure 3.8 shows the proposed solution for the update of the thrust balance, and in particular the position in respect to the pendulums. The arrangement of the original Item

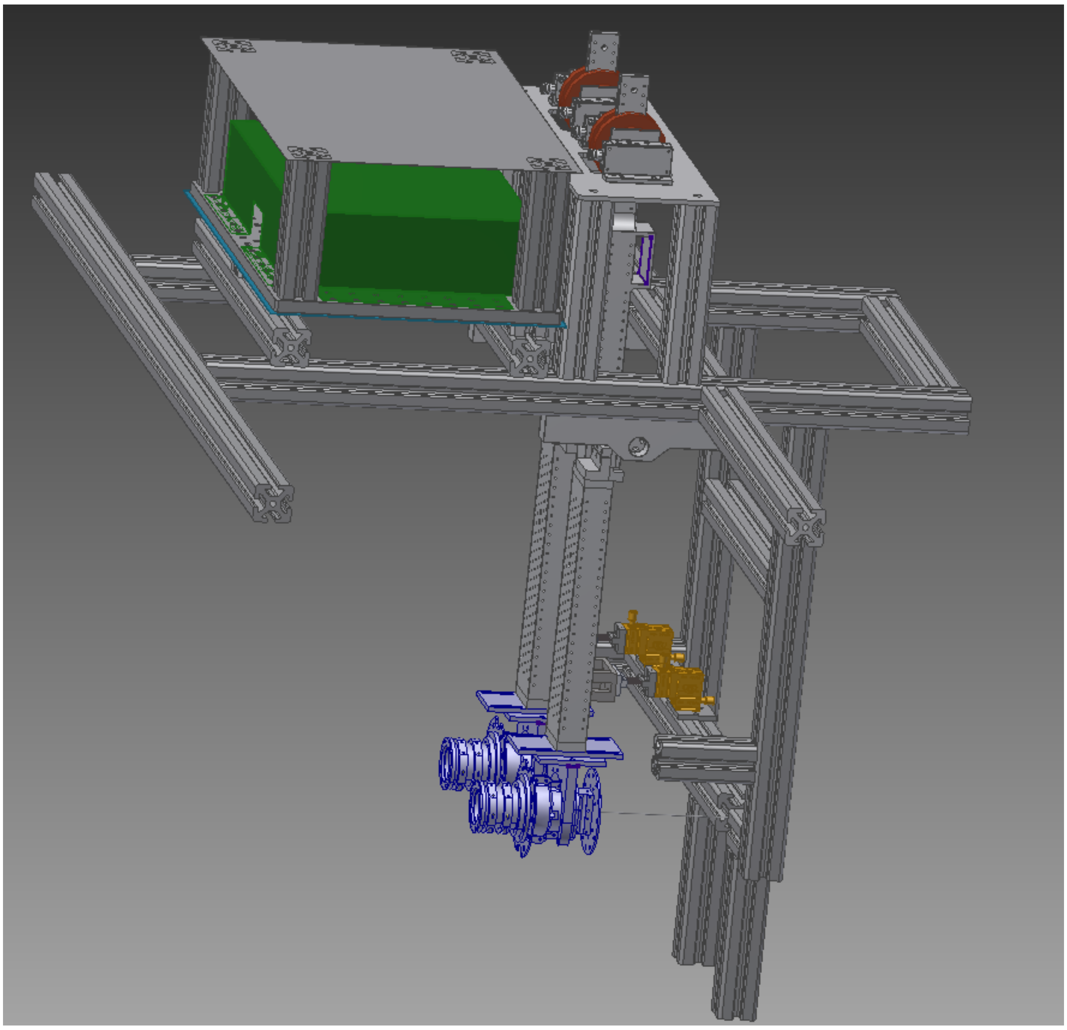

Figure 3.8: Proposed architecture for the updated balance. The disposition of the Item profiles is slightly changed to accommodate the size of the new breadboard, and two thermal protection plates can be added to further protect the setup. A comparison can be made with Figure 3.4

profiles needs to be slightly modified to accommodate the new breadboard, and to be able to use the new connections made by cutting Item profiles. Moreover, it is possible to see the cover for the whole setup, and the suggested thermal protection plates both on top and below the breadboard.

Since the functionality of the differential measurement needs to be assessed, but it was not possible to directly remove the previous interferometer, the setup is assembled on the breadboard, and two external mirrors are mounted in front of the devices. The two devices are connected to the breadboard using the connections introduced in Figure

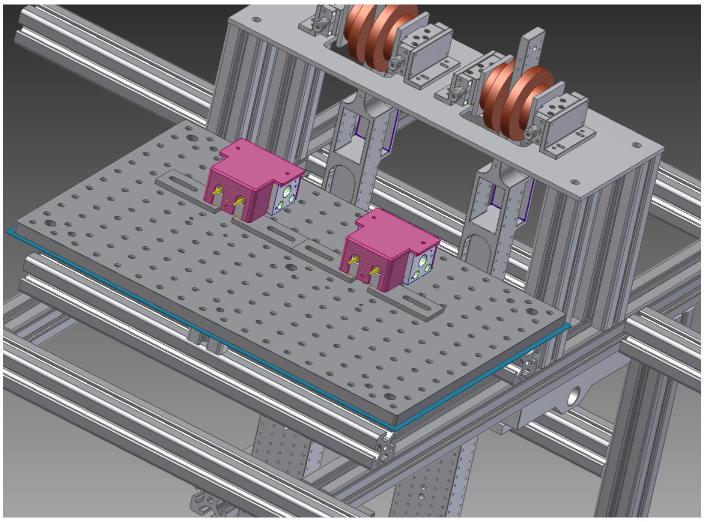

Figure 3.9: Detail of the interferometers position on the balance structure. The devices are positioned so that the laser beam hits as close as possible to the center of the mirror on each pendulum. A comparison can be made with Figure 3.4

3.6, and consolidated in the final position; the connections are used at particular angles to allow for the whole setup to be shrouded by the chamber cover. The fibers are connected to the fiber taps, which are then looped through a custom made cylindrical structure; during this process, it was imperative to avoid creating loops that were too small with the fibers, to avoid damaging the light transmission. Moreover, to better separate them, a cushion-like material was used in between the fibers; this provided also an interruption in the heat flow, therefore reducing the stress on the fiber core. The end of the fiber taps are mounted on supports close to the opening in the external cover, to allow for faster and easier fiber connections and substitutions, if necessary.

The USB cables that carry the data from the PCBs to the external computer are inserted in a USB hub; this is also provided with an external power supply, to ensure the nominal 5V voltage on the circuit. The test setup is shown in Figure 3.10.

The laser beams are provided by the frequency generation setup of the current interferometer; the chosen beat frequency is set to 20 kHz, and the amplitude of each beam is chosen to balance the power of each beam on the photo-detectors and to achieve the highest contrast possible. In air, the contrast can be estimated as 93% for both devices. Since the preliminary tests are performed in air, the noise of the measurements is higher

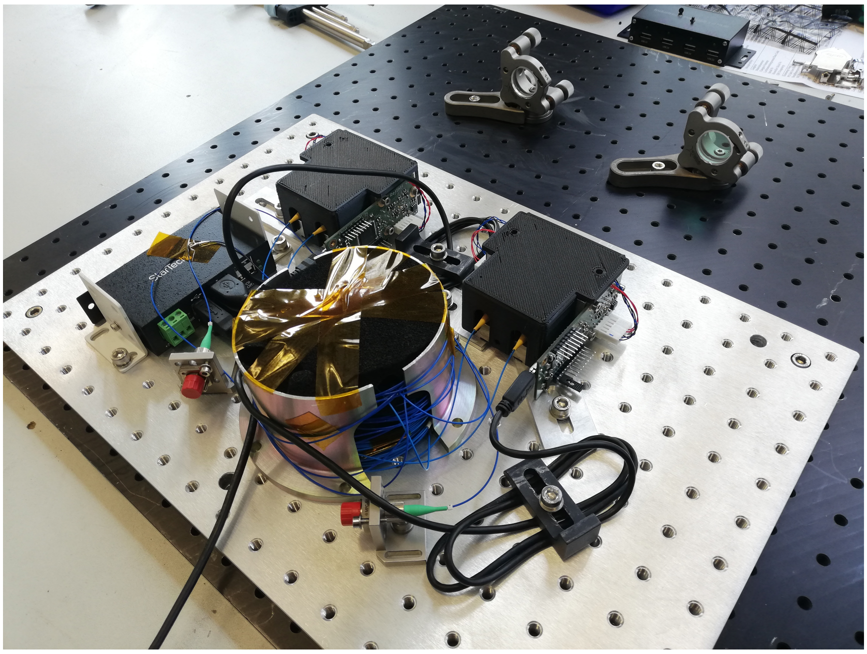

Figure 3.10: Test setup for the initial assessment of the updated interferometer. The two devices are connected to the breadboard using the connections introduced in Figure 3.6, and consolidated in the final position. The fibers are looped inside a cylindrical structure both for protection and space optimization purposes. Two external mirrors are placed at an appropriate distance to simulate the thrust balance pendulums.

than in vacuum; however, they provide an indication of the correct operation of the setup without the complications associated with providing the vacuum environment. In particular, one measurement demonstrated the validity of the double device architecture, as the drift in the path length measurement is compensated by performing the differential evaluation (Figure 3.11).

Due to some difficulties related to the measurements, it was decided to perform a test using an amplitude modulation to assess the correct operation of the phasemeter microcontroller; the test is performed in air, using a frequency of 20 kHz and a depth of 100%. Since the measurement is carried out in air, the results are expected to be slightly worse than the ones previously achieved in vacuum (however the amplitude modulation is able to suppress most of the effect of the air movement). The test provided acceptable results, which are summarised in Figure 3.12; this graph describes the noise associated with the differential path length measurement, which is adequate considering the noise

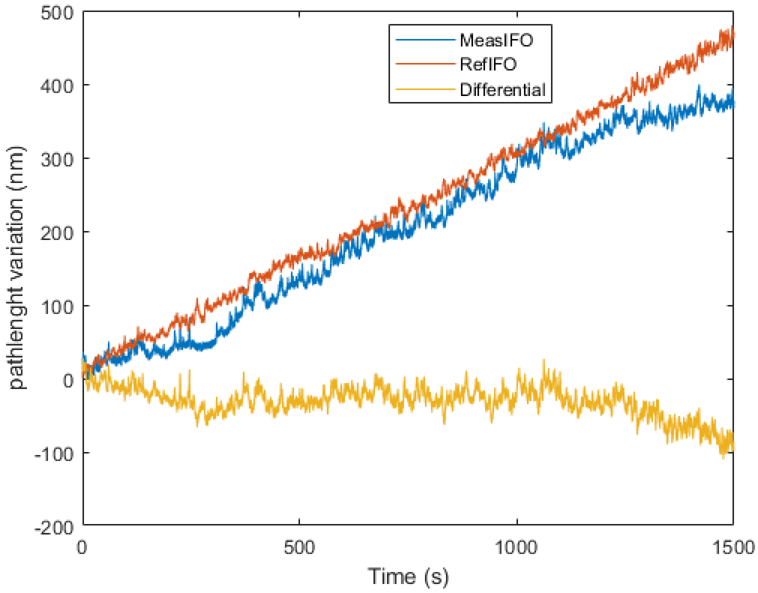

Figure 3.11: Demonstration of the compensation of the drift in the differential measurement. The measurement was performed with a beat frequency of 20 kHz.

caused by the presence of air and the laser frequency noise. In particular, the test allowed for the confirmation of the correct operation of the microcontroller, which would not have produced such results if damaged or malfunctioning.

To complete the preliminary characterisation of the setup, a test in vacuum is performed; the measurement captured data for around 14 hours and produced encouraging results.

- the contrast achieved outside of vacuum does not change to unacceptable levels; the reference interferometer maintains a contrast of about 85%, while the measurement interferometer stops around 78%

- the differential measurement is able to suppress much of the deviations, as already demonstrated more than once, and the noise from this measurement is smaller than the noise produced by the single devices

- the feedthrough connections correctly operate to provide the exchange of energy, light and data

- the noise levels of the differential path length measurement are below 1 nm/$\sqrt{\text{Hz}}$

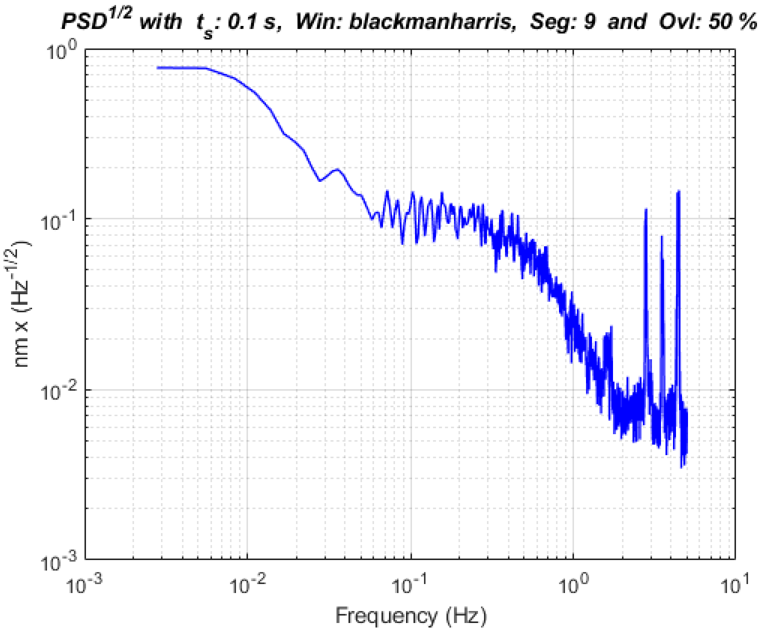

Figure 3.12: Noise characterisation of the differential path length measurement with an amplitude modulation (20 kHz, 100% depth), in air. This test allowed for confirmation of the correct operation of the microcontroller on both interferometers.

between 3 mHz and 1 Hz, which is quite close to the ideal performance (below 1 nm/$\sqrt{\text{Hz}}$ between 1 mHz and 1 Hz)

The results for this measurement are shown in Figure 3.13.

3.3.1 Power Spectral Density (PSD) diagrams [32–34]

Spectral estimation is the process of estimating the amplitude composition of a signal as a function of frequency. The output of this process is usually called a Power Spectral Density (PSD), but it could also be presented in the form of Amplitude Spectral Density (ASD). It is important to emphasize the estimation characteristic of such a technique; the results form this kind of calculation, applied to real-world data, will necessarily constitute an approximation. As an example, a signal could be composed of a sinusoidal function, with a certain frequency and amplitude, and white noise with a certain density. The wanted output from the analysis that is conducted would be two graphs; one would describe the amplitude of the signal, and one the level of the noise floor. The *spectrum* of the signal is the amplitude characteristics, while the *spectral density* describes the noise floor level; the spectral density can be *linear* or referred to the *power*. The power spectral density

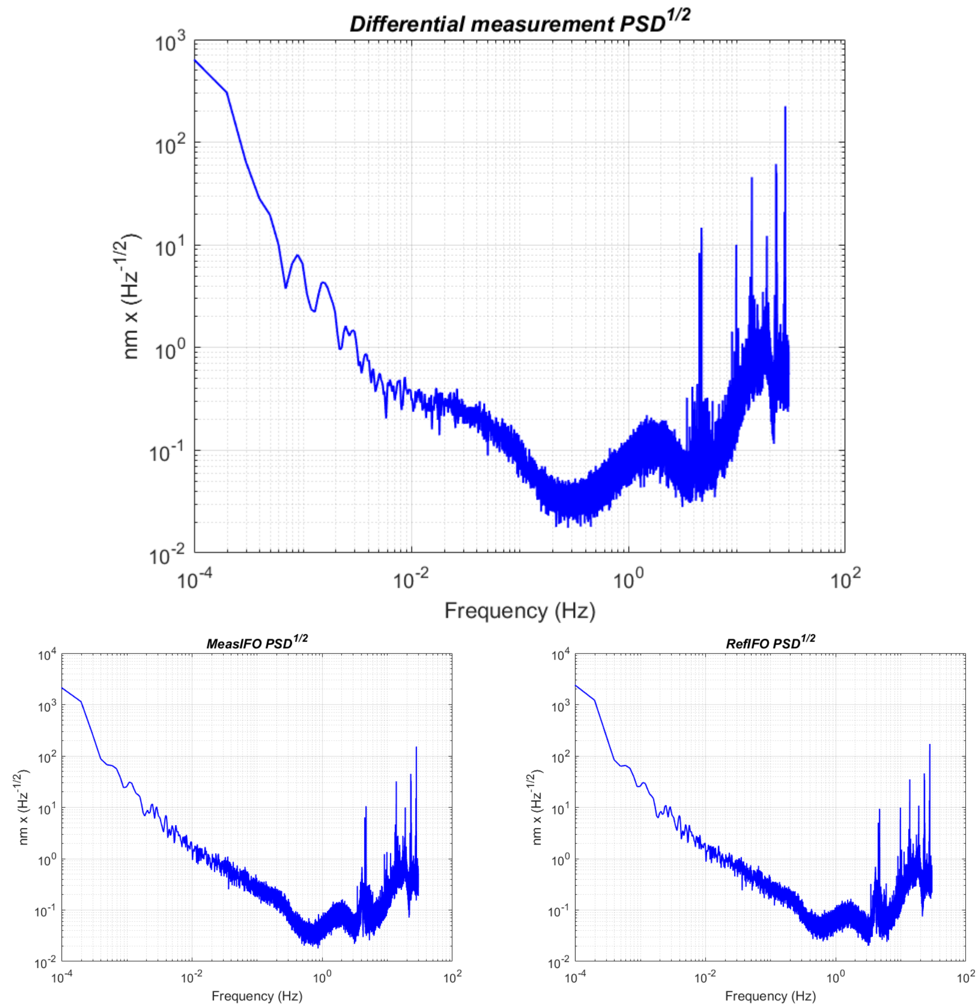

Figure 3.13: PSD diagrams for the overnight vacuum test of the completed setup; it is important to notice how the differential measurement noise is below 1 nm/$\sqrt{\text{Hz}}$ between 3 mHz and 1 Hz, which is quite close to the ideal performance. The comparison with the PSD diagrams of the single devices highlights how the noise is reduced by the differential measurement.

describes how the power of a time series is distributed with frequency; the linear spectral density is the square root of the power spectral density.

The tracing of the diagrams relies on the Discrete Fourier Transform of the signal; essentially, the signal is compared to a series of sinusoids with increasing frequency, and the portions that correspond to each sinusoid are summed to form a "bin" centered at the frequency of the pattern sinusoid. They are called frequency bins because an FFT can be seen as a set of parallel filters, with the same bandwidth Δf, each centered at a constant frequency increment. A full spectrum is constructed with a series of such bins.

The number of acquired points directly impacts the frequency resolution; for the same sampling frequency and for a given frequency range, increasing the number of acquired points allows for a higher frequency resolution.

$$\Delta f = \frac{f_s}{N} \tag{3.1}$$

To avoid aliasing problems, the sampling frequency needs to adhere to the Nyquist criterion, so its value needs to be at least twice the maximum frequency component in the signal.

Spectral Leakage: if, in a signal time series, there aren't an exact integer number of cycles then there will be a discontinuity in the signal at the end of the time series. In the frequency domain, the signal is not an integer multiple of the frequency resolution (or bin width). Spectral leakage causes the energy from a given frequency component to be distributed over adjacent frequency bins, therefore distorting the results.

This effect can be reduced by using a technique called "time domain windowing".

Windows: a window function weighs a time series to remove the discontinuities at the start or at the end, thus reducing the spectral leakage. Essentially, the spectrum of the original signal is combined with the spectrum of the window, a continuous spectrum with a main lobe (centered at each frequency component) and a number of side lobes. The side lobes near zero at regular intervals on each side of the main lobe. When an integral number of cycles is acquired, side lobes do not appear; instead, if the number of cycles is not integral, the side lobes appear on the spectrum and there is a certain amplitude error at the frequency peak, since the main lobe is shifted from its center and therefore sampled in this position.

The frequency resolution is affected by the choice of window function; it improves as the main lobe of the window narrows. However, this also causes more energy to be spread to the side lobes, thus worsening the spectral leakage.

Therefore, the selection of the window to apply needs to consider the requirement for a trade-off between the frequency resolution and the spectral leakage reduction. For the data

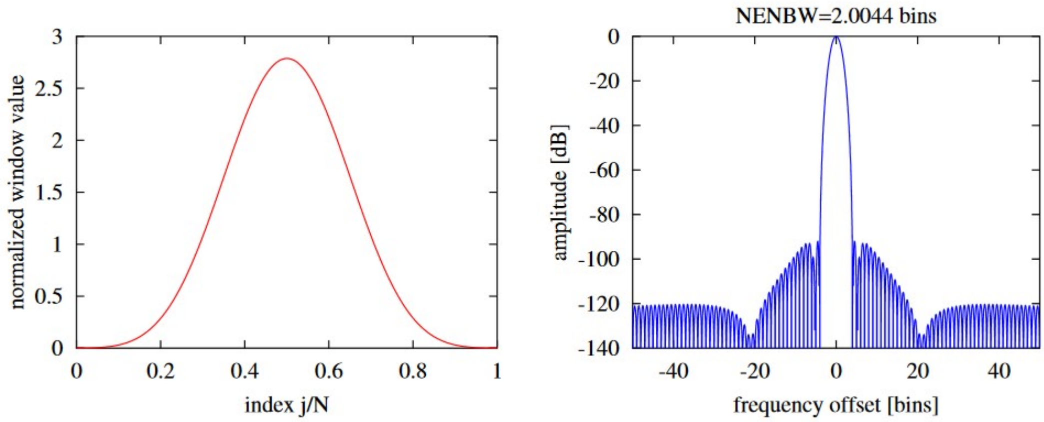

Figure 3.14: (92 dB) Blackman-Harris window function characteristics [34]

measured within this work, the Blackman-Harris window was used; the characteristics are summarized in Table 3.3.

-3 dB Main Lobe Width (bins)	1.62
-6 dB Main Lobe Width (bins)	2.27
Maximum Side Lobe Level (dB)	-71

Table 3.3: (71 dB) Blackman-Harris window function characteristics [33]

The Blackman-Harris window derives from the sum of cosine terms and is designed to have a small sidelobe adjacent to the main peak in the transfer function. It has a very small spectral leakage, but a reasonable bandwidth and amplitude error. It is used for detecting small sinusoidal signals which are close in frequency to larger signals.

Overlap: to apply a window function to a long, continuous stream of data, it could be beneficial to divide it into segments. However, since the window functions typically reach a value close to zero at the boundaries, part of the information is lost when applying the windows. If the windows overlap at least partially, this effect is reduced; the entity of the overlap is imposed by the kind of window (higher for narrower windows)

In this work, the PSD graphs that are presented have the following characteristics:

- sampling time of 0.1 s
- Blackman-Harris windows

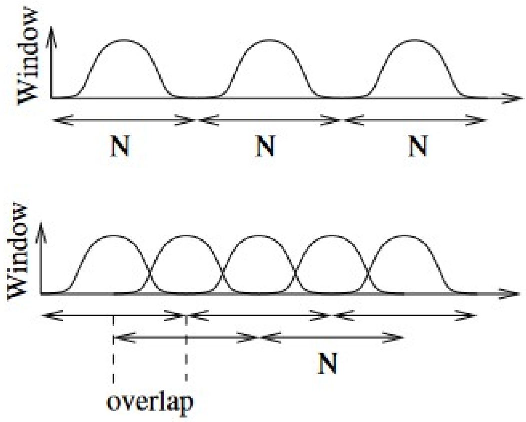

Figure 3.15: Segmented data stream with window and withwithout overlap [34]

- 50% overlap

Chapter 4

Conclusions and future prospects

This thesis work aimed to build and install a new interferometer device to substitute the one currently used by the Laboratory for Enabling Technologies in Airbus DS to evaluate the differential displacement between the two pendulums of the micro-Newton thrust balance during direct thrust measurements. The device was successfully assembled and characterised, as discussed in the previous chapters. The presence of such improved technology proves promising to enhance the capabilities of the testing facility.

In Chapter 2, a detailed explanation of the interferometer integration process was presented, along with the main results; the procedure that is described in this chapter allowed to demonstrate positive results for the implementation of the beamsplitters alignment software, as well as the achievement of a fully functional device. It was also possible to finalize the steps that are necessary for the construction of the devices, and to correct those that had issues undetected during the design phase. The vacuum tests that were performed show encouraging results in terms of signal-to-noise ratios; they also demonstrated the capability of the device to maintain a good alignment during the transition between ambient pressure and vacuum environment.

Moreover, it was shown that the construction process for the interferometer device could be performed in an iterative manner, producing several devices in a few months. As it was mentioned at the outset of the thesis, the device that was built and used within the thrust balance update was originally designed for another purpose; the original project

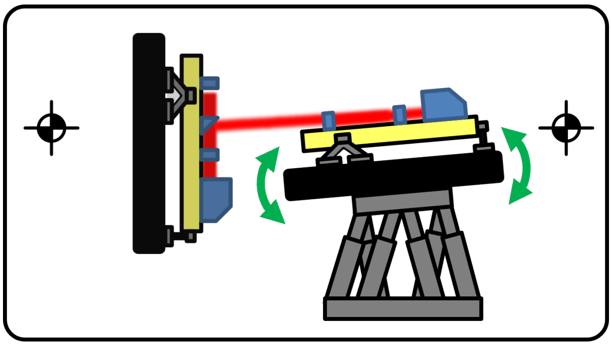

Figure 4.1: Future application of the interferometer device. It will be used to create multiple OMTs, one of which will be mounted on an exapod to achieve movement along 6 degrees of freedom. [21, 22]

aims to build on the results of a previous study to improve the understanding of the effects of relative motion between satellites in missions that require Interferometric Laser Ranging (such as LISA and GRACE-FO). For this purpose, an Optical Metrology Terminal (OMT) was developed; as an input, the setup receives a simulation of a laser beam received from a faraway spacecraft, while a reference interferometer tracks the path length variations caused by coupling effects. Expanding on this work, the aim is to build an Optical Formation Metrology Testbed (OFMT), in which an OMT is mounted on a freely movable platform (an hexapod) in order to better simulate the position errors between the satellites. Achieving such a test setup requires a certain number of the interferometers that were built as a part of this work; therefore, the success in completing the integration process proves vital for the OFMT research. [26, 30, 31]

In Chapter 3, the proposed design for the installation of the new interferometer in the thrust balance was presented, and the main results from the preliminary tests were shown. It was demonstrated that the two interferometers were able to provide a differential measurement which compensated for many noise sources, and that the software interface that was developed for the data acquisition was fully operational. In particular, it was proven that the setup had the capacity of measuring the differential path length with noise levels under 1 nm/$\sqrt{\text{Hz}}$ in a wide frequency band (3 mHz - 1 Hz); this achievement is extremely promising for the performance enhancement of the thrust balance as a whole. Improvements to the micro-controller code also provided better noise levels at higher frequencies.

The most important results to be highlighted in this section are:

- the capacity for both devices to maintain the alignment to fair levels through the transition from ambient pressure to vacuum, which improves upon the current setup where alignment problems cause the contrast of the measurement to drop well under 50%. The new device structure is able to maintain contrast levels over 75% (and up to 85%)
- the noise associated with the differential path length measurement is very satisfactory, and very close to the ideal value of $< 1\ \mathrm{nm}/\sqrt{\mathrm{Hz}}$ between 1 mHz and 1 Hz
- the improvement on the phasemeter code allows for better results for the noise levels at higher frequencies
- the capacity for the DWS measurement is enhanced from the current interferometer, allowing for a better determination of the deflection of the measurement pendulum
- it was discovered that the new setup occupies less space in terms of the depth inside the chamber; this attribute liberates space that can then be used in the installation of other devices in the vacuum chamber to further improve the diagnostic capabilities

Appendix A

DLL for the LabView interface

```
#ifdef _WIN32
        #include <windows.h>
#else
        #include <unistd.h>
#endif

#include <stdint.h>
#include "phasemeter_device.h"
#include <stdio.h>
#include <math.h>
#include <vector>
#include <string>

#define EXTERN_DLL_EXPORT extern "C" __declspec(dllexport)

const unsigned int vendor_id = 0x1e8e;
const unsigned int product_id = 0x5751;

phasemeter_device* RefIFO = nullptr;
phasemeter_device* MeasIFO = nullptr;

std::vector<std::wstring> enumerate() {

        static std::vector<std::wstring> serial_list;

        serial_list.clear();

        struct hid_device_info *devs, *cur_dev;

        devs = hid_enumerate(vendor_id, product_id);

        cur_dev = devs;

        while (cur_dev) {
                std::wstring serial(cur_dev->serial_number);
                serial_list.push_back(serial);
                cur_dev = cur_dev->next;
        }

        hid_free_enumeration(devs);

        return serial_list;
}

EXTERN_DLL_EXPORT void getDeviceList(char* device1, char* device2) {

        std::vector<std::wstring> serial_list = enumerate();
```

```
        sprintf(device1,"%ls",(serial_list.size()>=1)?
                            serial_list[0].c_str():L"no_device");
        sprintf(device2,"%ls",(serial_list.size()>=2)?
                            serial_list[1].c_str():L"no_device");

}


EXTERN_DLL_EXPORT int connectReferenceIFO(char* serial) {
        if (RefIFO == nullptr) RefIFO = new phasemeter_device(vendor_id,product_id);
        std::wstring wserial (serial,serial+strlen(serial));
        return RefIFO->open(wserial);
}

EXTERN_DLL_EXPORT int connectMeasurementIFO(char* serial) {
        if (MeasIFO == nullptr) MeasIFO = new phasemeter_device(vendor_id,product_id);
        std::wstring wserial (serial,serial+strlen(serial));
        return MeasIFO->open(wserial);
}

EXTERN_DLL_EXPORT void disconnectReferenceIFO() {
        RefIFO->close();
}

EXTERN_DLL_EXPORT void disconnectMeasurementIFO() {
        MeasIFO->close();
}


EXTERN_DLL_EXPORT void readReferenceIFO(uint32_t* index, uint32_t* phase,
                                            uint32_t* frequency, uint16_t* DC_amplitudes,
                                                uint16_t* AC_amplitudes, uint8_t* status) {

        interferometer_hid_data_t data = RefIFO->read();

        *index = data.index;
        phase[0] = data.phase_q1;
        phase[1] = data.phase_q2;
        phase[2] = data.phase_q3;
        phase[3] = data.phase_q4;
        *frequency = data.frequency;
        memcpy(DC_amplitudes,data.amplitude_DC,sizeof(uint16_t)*5);
        memcpy(AC_amplitudes,data.amplitude_AC,sizeof(uint16_t)*5);
        *status = data.status_A;

}

EXTERN_DLL_EXPORT void readMeasurementIFO(uint32_t* index, uint32_t* phase,
                                            uint32_t* frequency, uint16_t* DC_amplitudes,
                                                uint16_t* AC_amplitudes, uint8_t* status) {

        interferometer_hid_data_t data = MeasIFO->read();

        *index = data.index;
        phase[0] = data.phase_q1;
        phase[1] = data.phase_q2;
        phase[2] = data.phase_q3;
        phase[3] = data.phase_q4;
        *frequency = data.frequency;
        memcpy(DC_amplitudes,data.amplitude_DC,sizeof(uint16_t)*5);
        memcpy(AC_amplitudes,data.amplitude_AC,sizeof(uint16_t)*5);
        *status = data.status_A;
}

EXTERN_DLL_EXPORT void convertPhase(uint32_t* phase, int32_t* cycleCounter, double* cycles) {
        for(int i=0; i<4; i++) {
```

```
                cycles[i] = phase[i]/4194304.0;
        }

        int fullCycles[4];
        double fractionalCycles[4];

        for(int i=0; i<4; i++) {
                fullCycles[i] = floor(cycles[i]);
                fractionalCycles[i] = cycles[i] - fullCycles[i];
                if((fullCycles[i] - (cycleCounter[i]&0x3FF))>=512) {
                        cycleCounter[i] = (cycleCounter[i]&(~0x3FF)) + fullCycles[i] - 1024;
                }
                else if(((cycleCounter[i]&0x3FF)-fullCycles[i])>=512) {
                        cycleCounter[i] = (cycleCounter[i]&(~0x3FF)) + fullCycles[i] + 1024;
                }
                else {
                        cycleCounter[i] = (cycleCounter[i]&(~0x3FF)) + fullCycles[i];
                }
                cycles[i] = cycleCounter[i] + fractionalCycles[i];
        }

}


EXTERN_DLL_EXPORT double resetPathLengthRefIFO(double averagePathLengthRefIFO,
                                                   double pathLengthOffsetRefIFO) {
        pathLengthOffsetRefIFO = averagePathLengthRefIFO;
        return pathLengthOffsetRefIFO;
}

EXTERN_DLL_EXPORT double resetPathLengthMeasIFO(double averagePathLengthMeasIFO,
                                                   double pathLengthOffsetMeasIFO) {
        pathLengthOffsetMeasIFO = averagePathLengthMeasIFO;
        return pathLengthOffsetMeasIFO;
}

//path length expressed in mm

EXTERN_DLL_EXPORT void resetReferenceIFODWS(double* dwsCycleOffsetRefIFO,
                                               double* cyclesRefIFO) {
        for(int i=0; i<3; i++) {
                dwsCycleOffsetRefIFO[i] = round(cyclesRefIFO[i+1]-cyclesRefIFO[0]);
        }
}

EXTERN_DLL_EXPORT void resetMeasurementIFODWS(double* dwsCycleOffsetMeasIFO,
                                               double* cyclesMeasIFO) {
        for(int i=0; i<3; i++) {
                dwsCycleOffsetMeasIFO[i] = round(cyclesMeasIFO[i+1]-cyclesMeasIFO[0]);
        }
}

EXTERN_DLL_EXPORT void calculateDWS(double* cycles, double* dwsCycleOffset,
                                       double* dwsX, double* dwsY) {
    *dwsX = 2000*M_PI * (cycles[2]-dwsCycleOffset[1]-cycles[3]+dwsCycleOffset[2]) / 3456.0;
    *dwsY = 2000*M_PI * (cycles[1]-dwsCycleOffset[0]-cycles[0]) / 3456.0;
        //the dws value is expressed in mrad, that is why the 1000 factor is needed
}
```

The DLL calls for another library, which was previously developed for the interferometer device. It contains the basic functions to connect, disconnect and read data from the interferometers. As can be noticed, it was decided to operate using different functions for each device; moreover, most of the functions do not return any value because the "Call

Function" nodes in LabView allow the use of a variable both as an input and as an output, and therefore all necessary values can be derived.

Appendix B

Laser generation	
NPRO Crystal	$T = 26.5°\text{C}$
Diode A	$i = 1.55A$, $T = 15.8°\text{C}$
Output power at 1064 nm	0.52 W
PZT Turning Coefficient	2.4 MHz/V

Table B.1: Mephisto 500 Laser System

Fiber Collimator 60FC-A11-80	
Lens type	A11
Focal length [mm]	11
Numerical Aperture (NA)	0.25
Clear aperture max. [mm]	5.5
Collimated beam diameter [mm]	1.97
Beam divergence [mrad]	0.22

Table B.2: Fiber Collimator 60FC-A11-80

UHU Plus Schnellfest

Time	**Shear Strength**
10 minutes	150 N/cm^2
30 minutes	900 N/cm^2
60 minutes	1100 N/cm^2
12 hours	1300 N/cm^2

Table B.3: UHU Plus Schnellfest. The shear strength is tested at room temperature [17]

UHU Plus Endfest

Temperature	Hardening time	Bond strength
40 °C	3 hours	18 N/mm^2
70 °C	45 minutes	20 N/mm^2
100 °C	10 minutes	25 N/mm^2
180 °C	5 minutes	30 N/mm^2

Table B.4: UHU Plus Endfest [18]

Interferometer cover manufacturing

Method	CNC machining
Material	Stainless steel 304/304L (X5CrNi18-10)
Surface finish	As machined (Ra 3.2 μm)
General tolerance	ISO 2768 fine

Table B.5: Specifications for the manufacturing of the interferometer cover

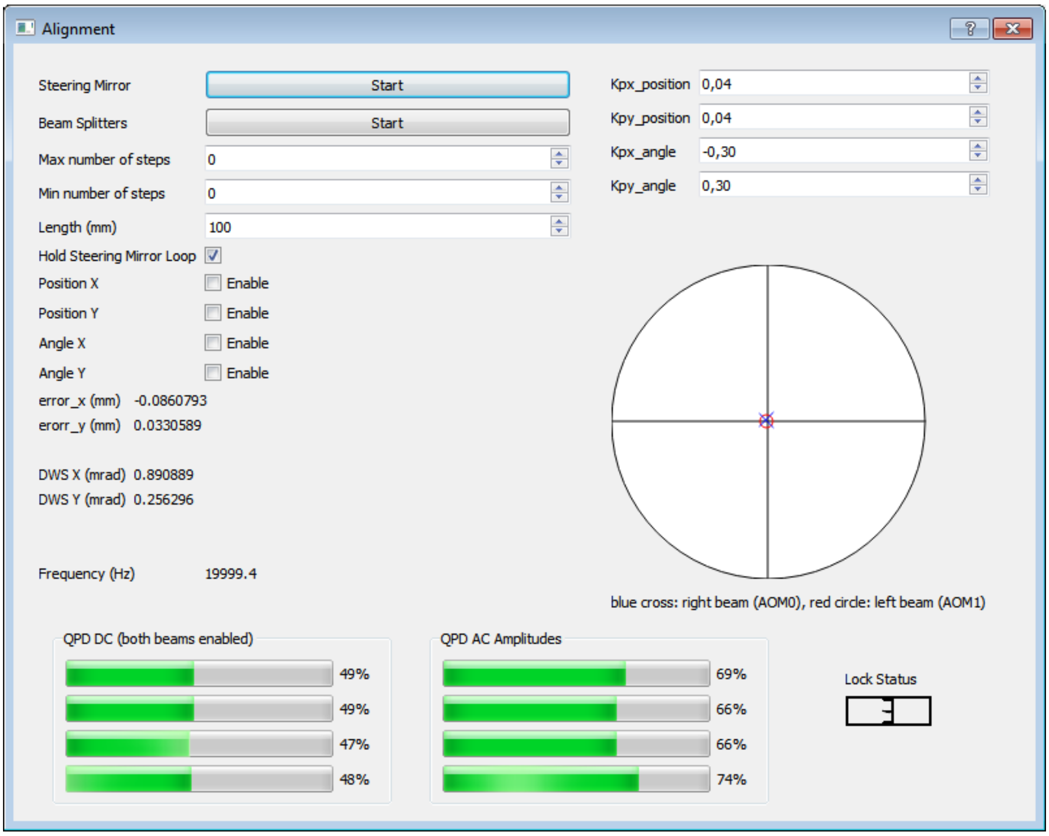

Figure B.1: Screenshot of the alignment program main window, where all the information described before can be easily seen on a graphical interface. In this case, the Lock Status is 3 because the source of the PLL is the single element photodiode, while it would be 7 for a locked PLL with the QPD as the source. [21, 26]

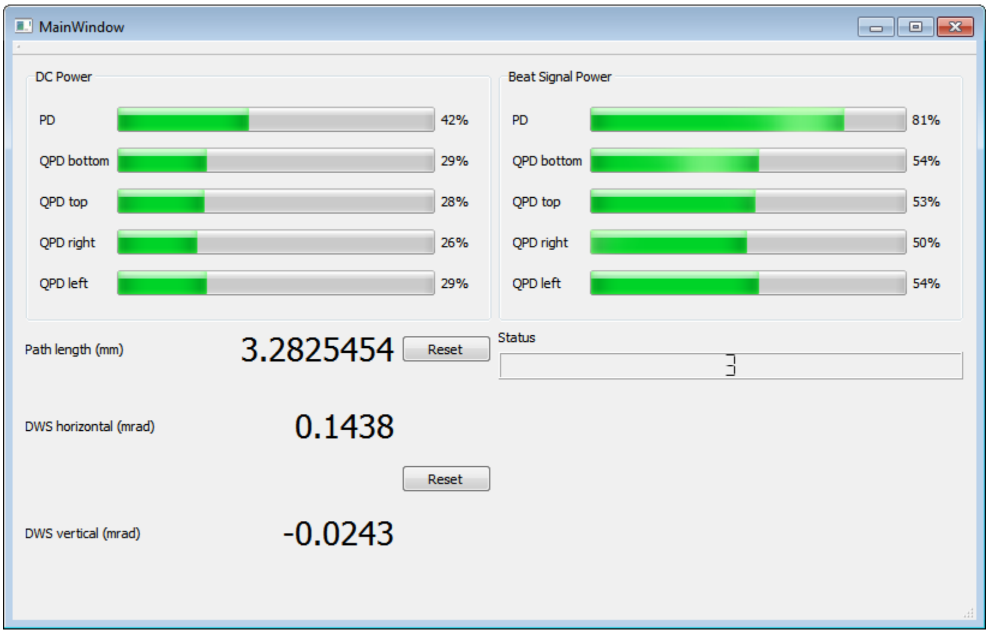

Figure B.2: Screenshot of the interferometer program main window. It is possible to see the DC and beat signal power, which are approximately correlated with a factor of two, the measurement for the DWS and the path length and the lock status (which is correctly 3 as the source for the PLL is the single element photodiode).

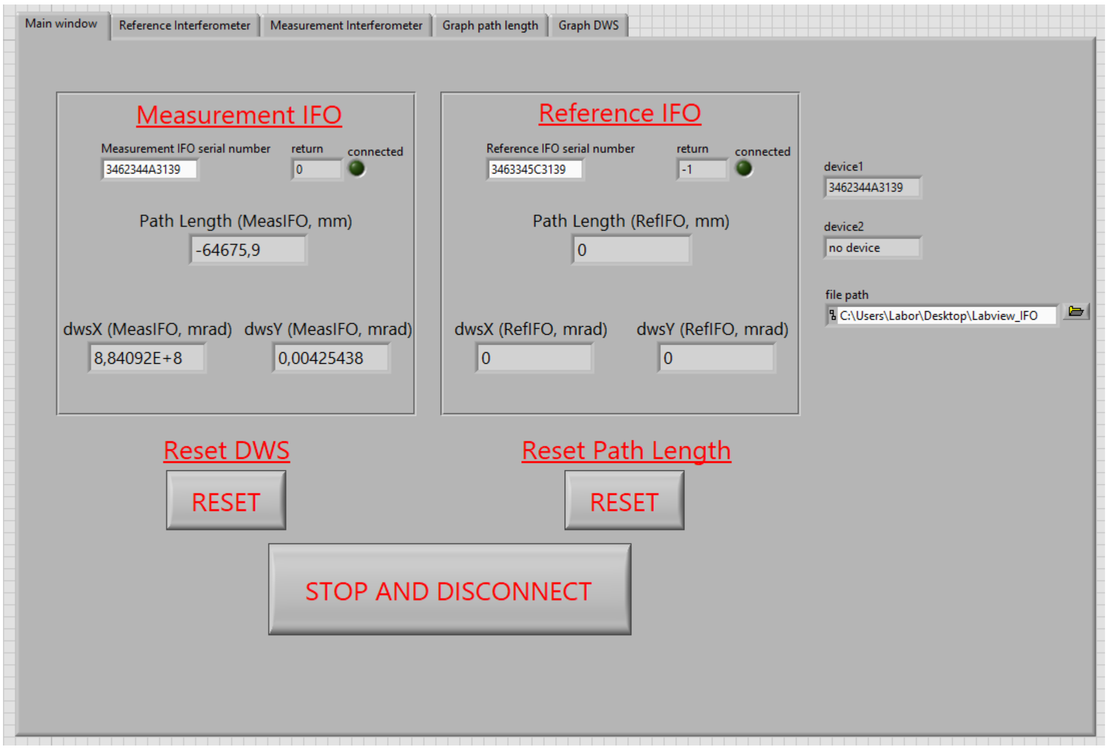

Figure B.3: Main window of the LabView user interface. It displays the fundamental information, and allows the user to reset the path length and DWS measurements; pressing the "Reset Path Length" button will update the offsets for both devices, and the same for "Reset DWS". To check if the connection of the device was successful, the "return" value should be equal to zero. The content of the second and third tab closely resemble the window used for the preliminary testing of the interferometer, with bars to display the AC and DC values, frequency and status.

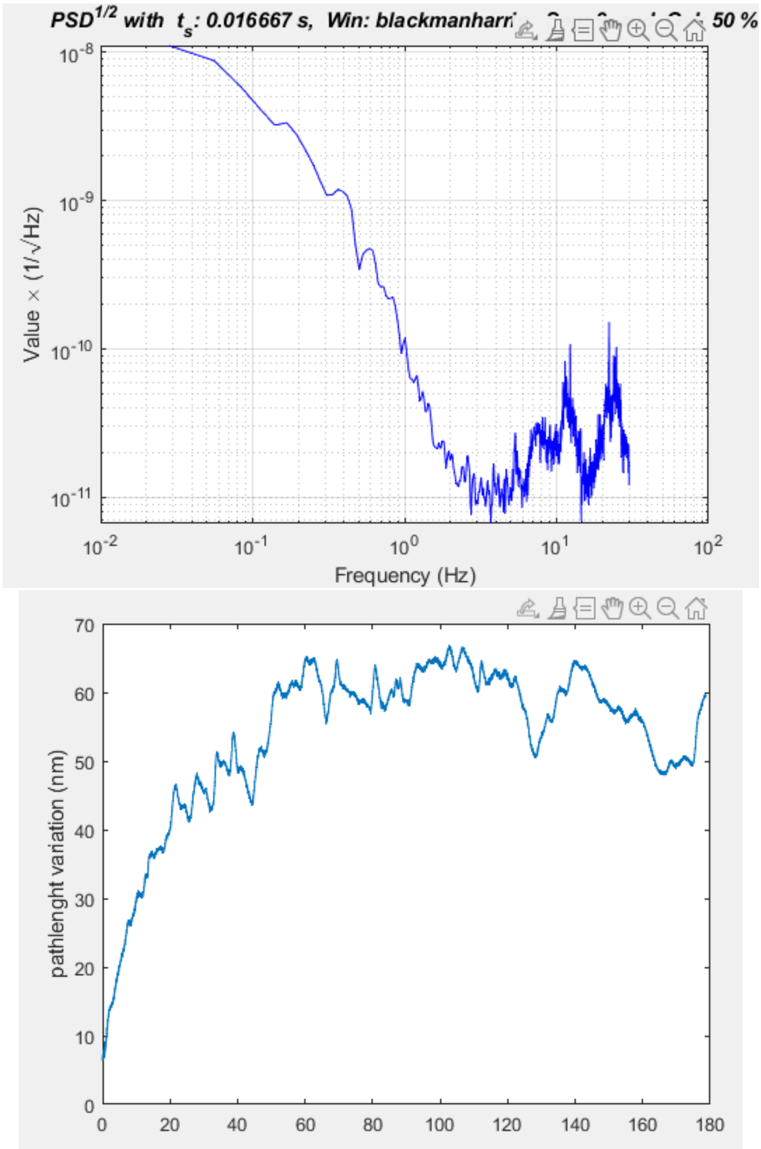

Figure B.4: Initial characterization results for the first interferometer; the first graph displays the frequency spectrum and the second graph displays the pathlength variation as a function of time. The complete characterization needs to be performed in vacuum, to avoid noise caused by the movement of air. [21]

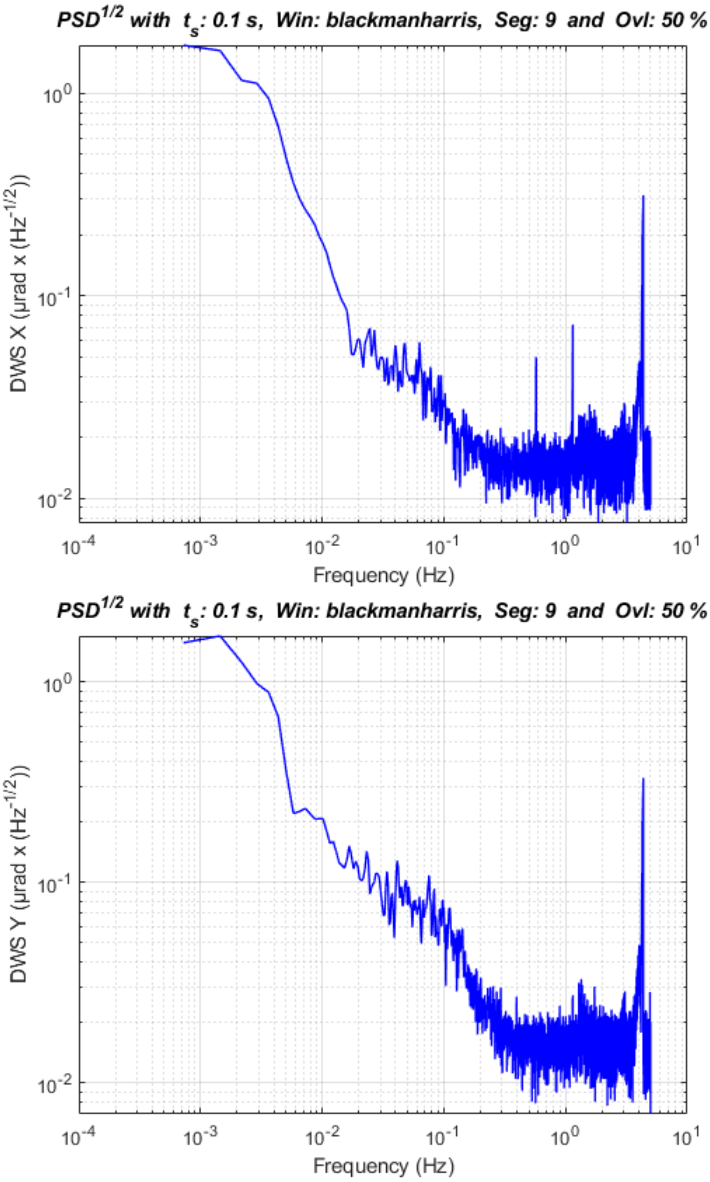

Figure B.5: Results from the measurement in vacuum using the amplitude modulation. The frequency was set to 20 kHz, and the depth of the sinusoidal signal to 100%. Refer to Figure 2.21

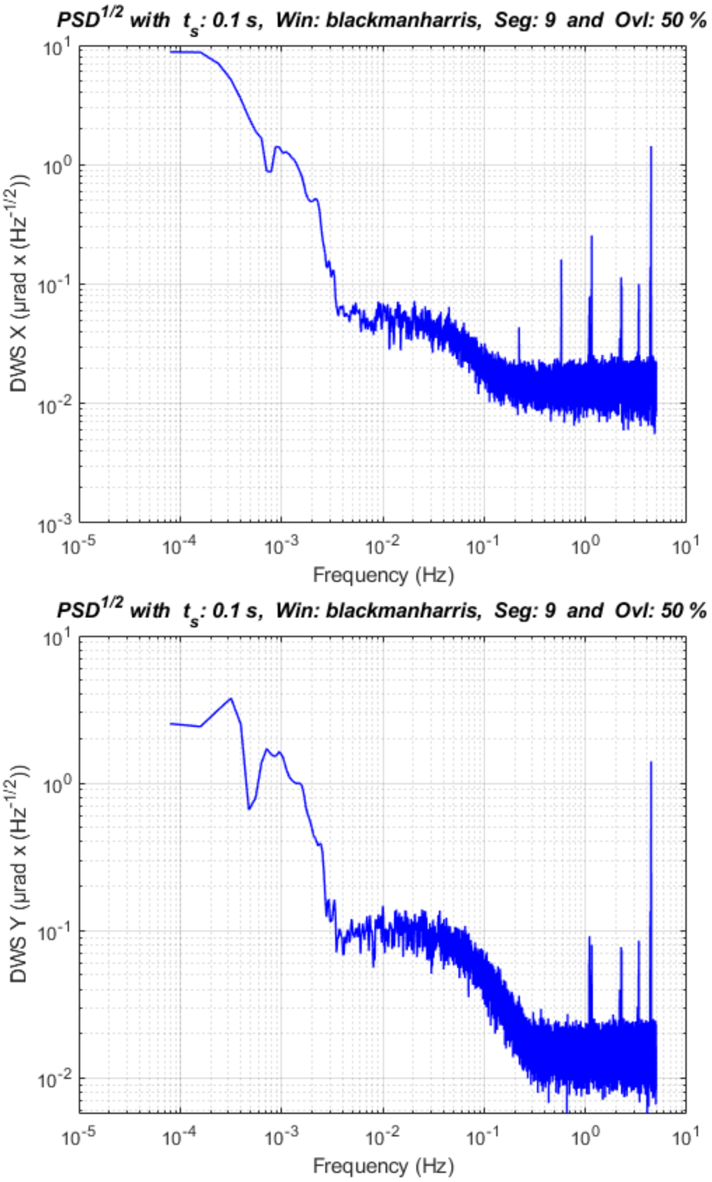

Figure B.6: Results from the overnight measurement in vacuum using the amplitude modulation. The frequency was set to 20 kHz, and the depth of the sinusoidal signal to 100%. Refer to Figure 2.22

Bibliography

[1] J. Gonzalez del Amo, G. Saccoccia, P. E. Frigot, *ESA Propulsion Lab at ESTEC*, presented at the 31st International Electric Propulsion Conference, University of Michigan, September 20 – 24, 2009

[2] J. E. Polk, A. Pancotti, T. Haag, S. King, M. Walker, J. Blakely, and J. Ziemer, *Recommended Practice for Thrust Measurement in Electric Propulsion Testing*, `https://www.ncbi.nlm.nih.gov/pmc/articles/PMC7839308/`, J Propuls Power. 2017 May; 33(3): 539–555, published online 2017 Apr 24

[3] Y. Zhang, D. Guo, Y. Yang, *Design and Experimental Validation of a Micro-Newton Torsional Thrust Balance for Ionic Liquid Electrospray Thruster*, `https://www.mdpi.com/2226-4310/9/10/545`, Aerospace 2022, 9(10), 545

[4] Zh. Zhang, G. Hang, J. Qi, Zu. Zhang, Zhe Zhang, J. Liu, W. Yang and H. Tang, *Design and fabrication of a full elastic sub-micron-Newton scale thrust measurement system for plasma micro thrusters*, Plasma Science and Technology, Volume 23, Number 10, 2021

[5] H. Xu, Y. Gao, Q. Mao, L. Ye, Z. Hu, K. Zhang, P. Song and Q. Li, *A compound pendulum for thrust measurement of micro-Newton thruster*, Rev. Sci. Instrum. 93, 064501 (2022)

[6] K. P. Zetie, S. F. Adams, R. M. Tocknell *How does a Mach-Zehnder interferometer work?*, Physics Department, Westminster School, London, January 2000

[7] *Optical detection techniques: homodyne versus heterodyne*, Renishaw plc (UK), 2002

[8] Edmund Optics, *Understanding waveplates and retarders*, Application Notes, August 2019, `https://www.edmundoptics.eu/knowledge-center/application-notes/optics/`

[9] Edmund Optics, *What are beamplitters?*, Application Notes, November 2012, `https://www.edmundoptics.eu/knowledge-center/application-notes/optics/`

[10] R. Paschotta, *Article on "Acousto-optic Modulators"* in the RP Photonics Encyclopedia, `https://www.rp-photonics.com/acousto_optic_modulators.html`

[11] D. J. McCarron, *A Guide to Acousto-Optic Modulators*, December 7, 2007

[12] ThorLabs Insights, *What factors affect the amount of light coupled into a single mode fiber?*, January 2020 `https://www.thorlabs.com/newgrouppage9.cfm?objectgroup_id=14205`

[13] Fibercore, *Mode Field Diameter (MFD)*, visited in September 2022, `https://fibercore.humaneticsgroup.com/services-support/fiberpaedia/m/mode-field-diameter-mfd`

[14] Schäfter+Kirchhoff, *Technotes - Fiber Optics: Polarization Maintaining Fibers (PM Fibers)*, `https://www.sukhamburg.com/support/technotes/fiberoptics/cablebasics/pmc.html`

[15] ThorLabs Insights, *How does polarization-maintaining fiber preserve linearly polarized light?*, September 2020

[16] Schäfter+Kirchhoff, *Polarization alignment for coupling into polarization-maintaining fibers*, `https://www.sukhamburg.com/support/technotes/fiberoptics/SK010PA/applications.html`

[17] UHU GmbH & Co., *Technisches Merkblatt, UHU PLUS SCHNELLFEST*

[18] UHU GmbH & Co., *UHU PLUS ENDFEST, Universal strong dual component epoxy adhesive*

[19] S. Cincotta, A. Neild, C. He and J. Armstrong, *Visible Light Positioning using an Aperture and a Quadrant Photodiode*, Monash University, Melbourne, Australia, 2017

[20] A. Vera-Marquina, A. Diaz Sanchez, J. Miguel Rocha-Pérez, D. Berman-Mendoza, Ivan Padilla, *Quadrant photodiode for electronic processing*, Proc. SPIE 7419, Infrared Systems and Photoelectronic Technology IV, 74190Z (27 August 2009)

[21] Courtesy of Dr. Oliver Mandel, Laboratory for Enabling Technologies, Airbus Defence & Space Gmbh, Immenstaad am Bodensee

[22] Courtesy of Paul Koschmieder, Laboratory for Enabling Technologies, Airbus Defence & Space Gmbh, Immenstaad am Bodensee

[23] Courtesy of Dr. Franz Georg Hey, Laboratory for Enabling Technologies, Airbus Defence & Space Gmbh, Immenstaad am Bodensee

[24] F. G. Hey, *Micro Newton Thruster Development; Direct Thrust Measurement and Thruster Downscaling*, 2018

[25] European Space Agency, *Lisa, Unveiling a hidden Universe*, ESA/SRE, 2011

[26] V. Camacho Molina, *Optical Metrology Terminal for Space Applications*, University of Bremen and Airbus Defence & Space, 2023

[27] T. Schuldt, M. Gohlke, R. Spannagel, S. Ressel, D. Weise, U. J. & C. Braxmaier, *Sub-Nanometer Heterodyne Interferometry and Its Application in Dilatometry and Industrial Metrology*, International Journal of Optomechatronics, 2009

[28] I. Collins, *Phase-Locked Loop (PLL) Fundamentals*, Analog Dialogue 52-07, July 2018

[29] N. Bellomo, M. Magarotto, M. Manente, et al., *Design and In-orbit Demonstration of REGULUS, an Iodine electric propulsion system*, CEAS Space J 14, 79–90 (2022) `https://doi.org/10.1007/s12567-021-00374-4`

[30] O. Mandel, *Optical Metrology Terminal for Satellite-to-Satellite Laser Ranging*, PhD thesis, Universitäat Bremen, 2022

[31] O. Mandel, D. Weise and M. Chwalla, *Reflective device for use in an optical measuring system*, U.S.Patent 10,317,277, 19 Oct 2017

[32] *Spectral Estimation for ~~Dummies~~ Experimentalists*, Presentation by LET in Astrium GmbH

[33] M. Cerna, A. F. Harvey, *The Fundamentals of FFT-Based Signal Analysis and Measurement*, National Instruments, July 2000

[34] G. Heinzel, A. Rüdiger and R. Schilling, *Spectrum and spectral density estimation by the Discrete Fourier transform (DFT), including a comprehensive list of window functions and some new flat-top windows.*, Max-Planck-Institut für Gravitationsphysik (Albert-Einstein-Institut) & Teilinstitut Hannover, February 15, 2002